

See discussions, stats, and author profiles for this publication at: <https://www.researchgate.net/publication/289521230>

All-dielectric metamaterials

Article in *Nature Nanotechnology* · January 2016

DOI: 10.1038/nnano.2015.304

CITATIONS

763

READS

6,906

2 authors:



Saman Jahani

California Institute of Technology

16 PUBLICATIONS 919 CITATIONS

[SEE PROFILE](#)



Zubin Jacob

Purdue University

180 PUBLICATIONS 6,215 CITATIONS

[SEE PROFILE](#)

Some of the authors of this publication are also working on these related projects:



Photonic skin-depth engineering using all-dielectric metamaterials [View project](#)



Optical Applications [View project](#)

All-dielectric metamaterials

Saman Jahani¹ and Zubin Jacob^{1,2*}

The ideal material for nanophotonic applications will have a large refractive index at optical frequencies, respond to both the electric and magnetic fields of light, support large optical chirality and anisotropy, confine and guide light at the nanoscale, and be able to modify the phase and amplitude of incoming radiation in a fraction of a wavelength. Artificial electromagnetic media, or metamaterials, based on metallic or polar dielectric nanostructures can provide many of these properties by coupling light to free electrons (plasmons) or phonons (phonon polaritons), respectively, but at the inevitable cost of significant energy dissipation and reduced device efficiency. Recently, however, there has been a shift in the approach to nanophotonics. Low-loss electromagnetic responses covering all four quadrants of possible permittivities and permeabilities have been achieved using completely transparent and high-refractive-index dielectric building blocks. Moreover, an emerging class of all-dielectric metamaterials consisting of anisotropic crystals has been shown to support large refractive index contrast between orthogonal polarizations of light. These advances have revived the exciting prospect of integrating exotic electromagnetic effects in practical photonic devices, to achieve, for example, ultrathin and efficient optical elements, and realize the long-standing goal of subdiffraction confinement and guiding of light without metals. In this Review, we present a broad outline of the whole range of electromagnetic effects observed using all-dielectric metamaterials: high-refractive-index nanoresonators, metasurfaces, zero-index metamaterials and anisotropic metamaterials. Finally, we discuss current challenges and future goals for the field at the intersection with quantum, thermal and silicon photonics, as well as biomimetic metasurfaces.

It has been a long-held belief that strong light–matter interaction at the nanoscale necessarily requires light to couple to additional degrees of freedom in matter¹. These degrees of freedom are available through the collective oscillation of free electrons in a metal (plasmons²) or the vibration of phonons in a polar dielectric material (phonon polaritons³). To harness these couplings, artificial electromagnetic media (or metamaterials) consisting of such plasmonic³ (mainly Ag and Au) or phonon-polaritonic (mainly SiC) building blocks⁴ have been designed. Nanostructures have been optimized to achieve a range of exotic electromagnetic responses, including negative magnetic permeability⁵ (magnetic metal, $\mu < 0$), negative refractive index⁶ ($n < 0$), zero refractive index⁷ ($n \approx 0$), optical chirality^{8,9} and hyperbolicity¹⁰. However, the cost of such an approach is the inevitable increase of light absorption in matter and the subsequent conversion of light into heat — an irreversible process that has impeded many practical device applications.

Recently, however, a different approach to nanophotonics has emerged. Metamaterials composed of all-dielectric, completely transparent building blocks in which light does not couple to plasmons or optical phonons have been shown to achieve all four quadrants of electromagnetic responses: $\varepsilon > 0$, $\mu > 0$; $\varepsilon < 0$, $\mu > 0$; $\varepsilon > 0$, $\mu < 0$; $\varepsilon < 0$, $\mu < 0$, where ε is electric permittivity¹¹ (Fig. 1a). This approach overcomes the critical issue of heat dissipation and could bridge the gap between fundamental nanoscience and devices¹². We stress the fundamental difference of dielectric metamaterials, which employ near-field coupling between subwavelength building blocks, from dielectric photonic crystals¹³, where wavelength-scale periodicity creates bandgap effects for light confinement.

In Fig. 1a, we summarize the first applications arising from the recent field of all-dielectric metamaterials. Inspired by the pioneering ideas of Leonard Lewin¹⁴, researchers have shown that nanoresonators made of completely transparent building blocks of high refractive index, such as silicon, germanium and tellurium, can achieve optical magnetism^{15–17} ($\mu \neq 1$), negative-index ($\varepsilon < 0$, $\mu < 0$) and zero-index^{18,19} ($\varepsilon \approx 0$, $\mu \approx 0$) response. A host of applications have consequently been demonstrated, including magnetic mirrors²⁰ ($\mu < 0$), reflectionless ultrathin sheets mimicking highly directional Huygens

sources^{21,22} and control of spontaneous emission in zero-index media^{19,23}. Coupled nanoscale resonators have led to spectrally selective electric field hotspots at the nanoscale^{24,25} for biosensing and energy applications^{26,27}. A fundamental difference from the traditional field enhancement seen in plasmonic structures is the achievement of not only electric field hotspots but also nanoscale magnetic hotspots exploiting magnetic Mie resonances in coupled dimers²⁸.

Another unique aspect of all-dielectric metamaterials lies in the large amount of possibilities for engineering the anisotropy of the media. Unlike natural materials, where the principal refractive indices for the two possible polarizations (extraordinary and ordinary) rarely exceed 10%, all-dielectric metamaterials can be engineered to have much higher index contrast. Once this index contrast is increased, it is possible to make all-dielectric metasurfaces^{29–31} that can function to spectrally mould the optical wavefront³² and control light polarization far beyond the capabilities of traditional diffractive or refractive optical elements. These anisotropic media can also guide and steer Dyakonov surface waves^{33–35} for information processing and confine light to the nanoscale^{36,37} without using metallic components³⁶ (Fig. 1b).

High-index nanoresonators

In an electric metal, the real component of the dielectric permittivity at optical frequencies is negative ($\varepsilon' < 0$). Analogously, in a magnetic metal, the real component of the magnetic permeability is negative ($\mu' < 0$). Though metallic building blocks seem essential for negative permeability or negative permittivity media¹¹, they suffer from high energy dissipation. This fundamental challenge can be overcome using all-dielectric nanoparticles made of high-index semiconducting materials, such as silicon, germanium or tellurium (Fig. 2a). When light with frequency below or near the bandgap frequency of the material hits a high-index nanosphere, both the magnetic and electric dipole resonances are excited, making the particle behave like a magnetic dipole (first Mie resonance) and an electric dipole (second Mie resonance)³⁸. The magnetic Mie resonance possesses unique circular displacement currents^{39–42} that enhance the magnetic field at the particle's centre at optical frequencies (Fig. 2b). A similar

¹Department of Electrical and Computer Engineering, University of Alberta, Edmonton, Alberta T6G 1H9, Canada. ²Birck Nanotechnology Center, School of Electrical and Computer Engineering, Purdue University, Indiana 47906, USA. *e-mail: zjacob@purdue.edu

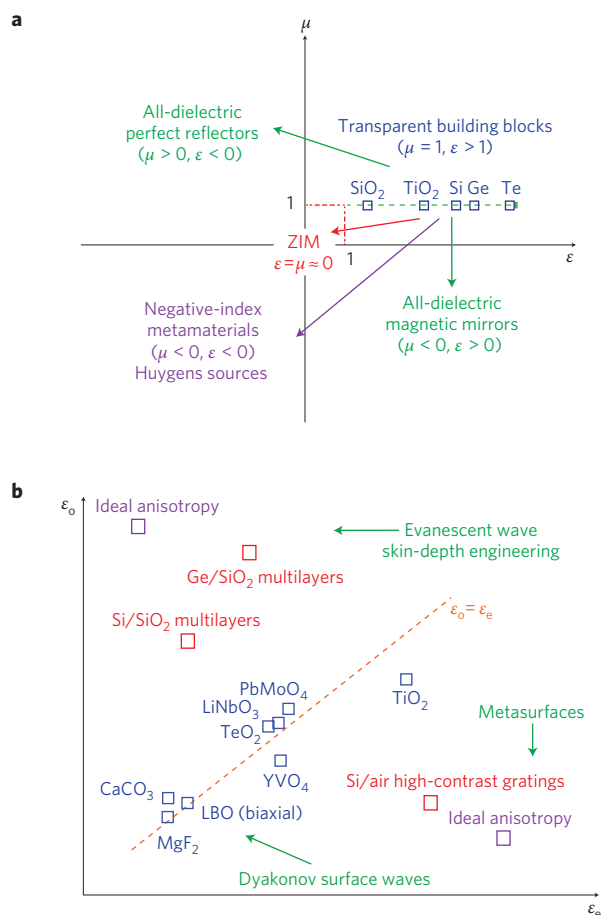


Figure 1 | Overview of isotropic and anisotropic all-dielectric metamaterials.

a, Electric permittivity (ϵ) and magnetic permeability (μ) form four quadrants that represent the entire range of the isotropic electromagnetic response. All four quadrants can be covered by designing specific all-dielectric metamaterials. ZIM, zero-index material. **b**, Extraordinary (ϵ_o) and ordinary (ϵ_e) permittivities ($n_e = \sqrt{\epsilon_e}$ and $n_o = \sqrt{\epsilon_o}$, where n is the refractive index) of natural anisotropic materials (blue squares) lie close to the line $\epsilon_o = \epsilon_e$ that represents isotropic materials. All-dielectric metamaterials with large anisotropy can be made using high-contrast gratings, high-index nanoresonators or multilayer superlattices with subwavelength thicknesses (red squares). Applications include metasurfaces to control the wavefront and polarization of light, waveguides for Dyakonov surface waves and evanescent wave skin-depth engineering for subdiffraction confinement without metals.

effect is observed in plasmonic split-ring resonators, which, however, only work at lower frequencies⁴³. These Mie resonances are accompanied by a characteristic resonant dispersion in the linear response regime¹⁴ (Fig. 2c), so an ensemble of spheres or an array of discs or cubes (metasurface) can be described by an effective negative dielectric permittivity at the electric resonance and by an effective negative magnetic permeability at the magnetic resonance⁴⁴ (Fig. 2c). Figure 2d shows the reflection and transmission spectrum from an array of cubic tellurium resonators with the two separate peaks and dips corresponding to the electric and magnetic resonances in the mid-infrared spectral range⁴⁵.

Immediate applications of Mie resonances in all-dielectric resonators include perfect reflectors^{46,47} and magnetic mirrors^{20,48–50}. The working principle of these optical devices is fundamentally different from conventional reflectors and mirrors. Silver and aluminium mirrors reflect most of the incoming light, but about 2% of

it is dissipated as heat. Bragg reflectors also function as good mirrors, but are hard to miniaturize and multilayer fabrication can be expensive. All-dielectric metasurfaces consisting of nanoscale high-index resonators achieve 100% reflection with subwavelength thickness at the resonant frequency, as demonstrated in the near-infrared spectral range using silicon nanoresonators^{46,47}.

It should also be noted that conventional electric mirrors not only reflect light but also impart a 180° phase reversal, causing destructive interference and an electric field minimum (node) right on the surface⁵⁰. This effect causes a strong suppression of light–matter interaction for emitters and absorbers placed in close proximity to the mirror surface. In contrast, magnetic mirrors exploiting magnetic resonances for reflections can sustain an electric field maximum on the surface (Fig. 2e). This arises because the electric field undergoes a zero phase change and the 180° phase reversal occurs only for the magnetic field. The zero phase reversal of an all-dielectric magnetic mirror made of high-index tellurium resonators ($n = 5.3$ at wavelength (λ) = $10\ \mu\text{m}$) was recently contrasted with the reflection phase of an electric mirror²⁰. This contrasting behaviour has been used at microwave frequencies to enhance antenna radiation efficiency near high-impedance surfaces⁵¹ and can have an important impact at optical frequencies for increasing light–matter interaction. Furthermore, magnetic mirrors are surprisingly tolerant to the disorder of nanoresonators on the metasurface due to the strong confinement of the photonic mode at the magnetic Mie resonance⁴⁷.

The rapid progress of all-dielectric metamaterials has been fuelled by the introduction of fabrication approaches beyond the conventional electron beam lithography and photolithography techniques. Spherical particles (Fig. 2f,g) cannot be fabricated using standard lithography techniques, while chemical methods lead to a broad distribution of particle sizes without precision in deposition⁵². In contrast, femtosecond laser ablation of a silicon wafer produces silicon nanoparticles and simultaneously induces a transfer process of these nanoparticles to a nearby glass substrate¹⁶. Interestingly, thin oxide layers or substrate effects do not change the spectral location of the sphere's Mie resonances. The size of such laser-ablated silicon nanoparticles is in the range of 100–200 nm, which produces Mie resonances in the visible frequency spectrum (Fig. 2f,g). Recent progress has been made on controlling the sizes, positions as well as crystallographic phase of the nanoparticles using an ultrafast laser-based melting and printing technique⁵³. A recent significant advance is the large-area fabrication (centimetre-size samples), in which over half a billion cylindrical silicon resonators were obtained using lithography with self-assembled polystyrene nanospheres⁴⁶.

Another application of high-index nanoresonators is in the emerging field of flat photonics^{29,30}. Metasurfaces made of plasmonic nanoantennas suffer from low transmission efficiency due to reflections and absorption⁵⁴. This fundamental drawback can be circumvented using all-dielectric metasurfaces. One important class of all-dielectric metasurfaces are reflectionless sheets, also known as Huygens metasurfaces^{21,22} (Fig. 2i). Christiaan Huygens explained the wave nature of light by assuming that radiation incident on an object produces tiny secondary sources of waves. However, the critical assumption was that these sources radiate only in the forward direction. Neither electrical nor magnetic dipoles possess this property. Interestingly, a source consisting of both electrical and magnetic dipole moments oriented perpendicular to each other radiates unidirectionally⁵⁵. This high directionality can be observed in all-dielectric single nanoparticles⁵⁶ or nanodiscs consisting of spectrally overlapping electric and magnetic Mie resonances¹⁷ (Fig. 2j). An array of such resonators (Fig. 2i) behaves like an array of Huygens sources with highly suppressed backward scattering (reflectionless sheets). Figure 2h shows the forward-to-backward scattering ratio measured using dark-field spectroscopy and the large suppression of the backward scattering for individual silicon spheres⁵². These

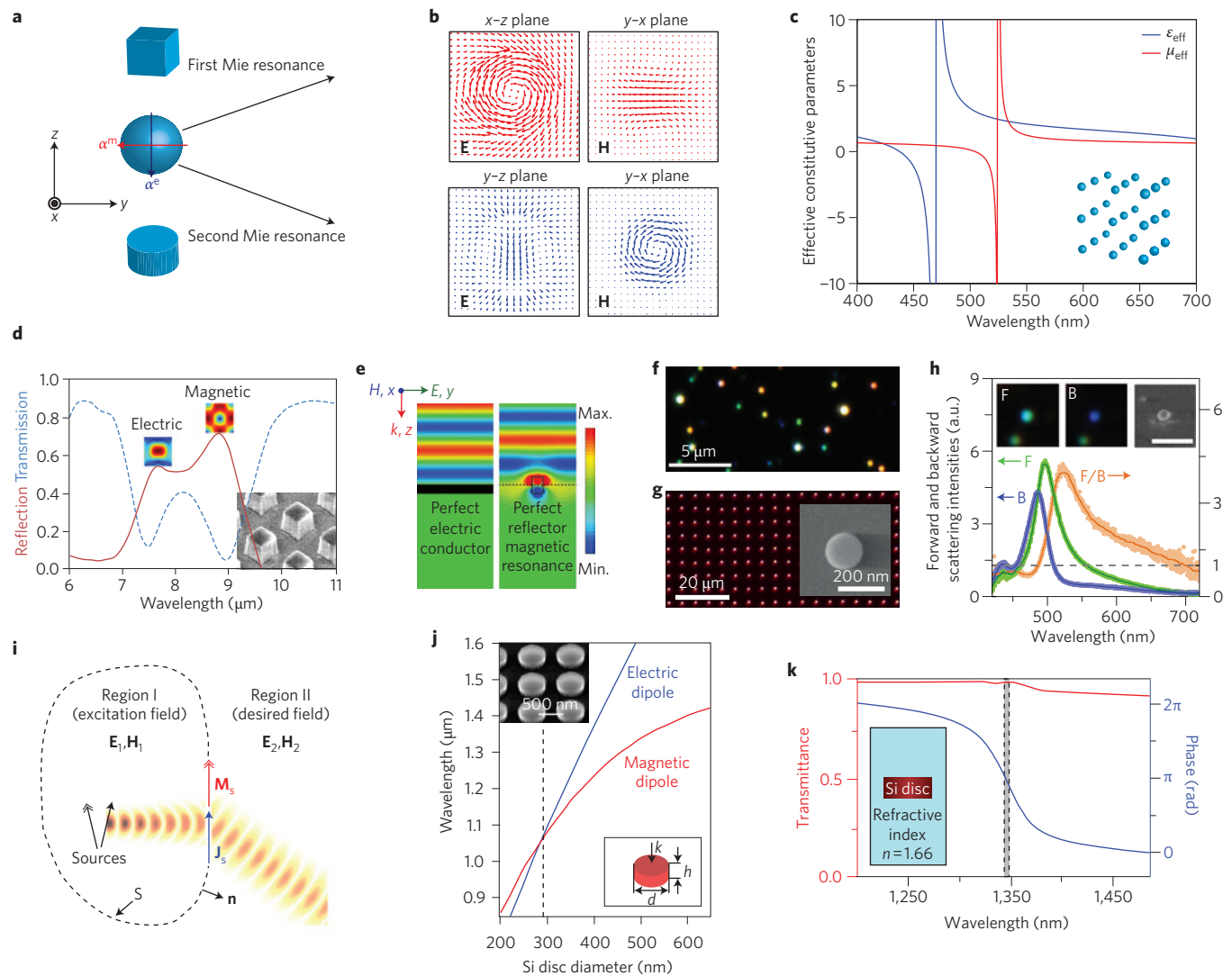


Figure 2 | High-index resonators. **a**, Cubic, spherical or disc-shaped resonators composed of a high-index dielectric show strong electric and magnetic resonances, which behave like electric (α^e) and magnetic (α^m) dipoles oriented perpendicular to each other. **b**, The electric and magnetic field distribution of the first and second Mie resonances of a spherical dielectric resonator. $\epsilon = 40$ and radius, $r = 0.5$ cm. The magnetic (H) and electric (E) resonances occur at frequencies $f = 4.73$ GHz and $f = 6.55$ GHz, respectively. The circular displacement current in the x - z plane is indicative of a magnetic dipole moment along the y direction. These resonances can be moved to the visible using 200 nm silicon nanospheres⁴⁴. **c**, The effective permittivity (ϵ_{eff}) and permeability (μ_{eff}) of a 3D array of spherical dielectric resonators (inset) with $\epsilon = 12$, $r = 150$ nm and a sphere volume fraction of $v_f = 0.3$. The magnetic and electric resonances correspond to an effective negative magnetic permeability and an effective negative dielectric permittivity. **d**, In the vicinity of electric or magnetic resonances, a 2D array of high-index tellurium resonators (inset; cube dimension = 1.45 μm) behaves like an electric or magnetic mirror, respectively. Silicon disc resonators can increase the efficiency of reflection on resonance to 100%⁴⁵. **e**, Contrasting electric field profiles of electric and magnetic mirrors. There is an electric field maximum at the surface of the magnetic mirror causing an enhancement in light-matter interaction since the reflection phase is zero⁴⁶. **f**, Experimental observation of magnetic resonances at visible frequencies for silicon nanospheres. The fabrication method is based on laser-induced transfer of nanoparticles melted by tightly focused laser pulses¹⁶. **g**, Laser ablation technique to produce silicon nanospheres. In both **f** and **g**, the scattering spectra have been measured using dark-field spectroscopy. The size of the nanoparticles is in the range of 100–200 nm (ref. 53). **h**, Interfering electric and magnetic Mie resonances leads to directional scattering from nanospheres and strong suppression of backward scattering. F/B, forward-to-backward scattering ratio. Insets: Images of the forward (F) and backward (B) scattered light and scanning electron microscope image of a nanosphere. Scale bar, 500 nm. The peak of scattered intensity occurs at different wavelengths for forward and backward scattered light manifested in the different colours of the images⁵². **i**, Huygens metasurfaces. Independent electromagnetic field distribution in different regions ($\mathbf{E}_{1,2}$, $\mathbf{H}_{1,2}$) can be achieved if electric (\mathbf{J}_s) and magnetic (\mathbf{M}_s) current sources at the surface S between the two regions are used to satisfy the boundary conditions. \mathbf{n} is the normal vector to the surface. Overlapping electric and magnetic resonances of equal strength can lead to current sources with directional radiation patterns known as Huygens sources²¹. **j**, The diameter (d) of silicon disc resonators can be tuned to exhibit the electric and magnetic resonances at the same frequency and achieve Huygens metasurfaces. The height (h) is 220 nm and the disc is embedded in a low-index dielectric ($n = 1.5$). Strong front-to-back ratio scattering is observed at resonance¹⁷. **k**, Calculated transmission intensity and phase response for silicon nanodiscs embedded in a medium with refractive index $n = 1.66$ (inset). Electric and magnetic resonances overlap at $\lambda = 1,340$ nm. More than 99% transmission and full phase coverage of 2π is achievable for arbitrary wavefront shaping²². Figure reproduced with permission from: **b**, ref. 44, APS; **d**, ref. 45, APS; **e**, ref. 46, American Chemical Society; **f**, ref. 16, Nature Publishing Group; **g**, ref. 53, Nature Publishing Group; **h**, ref. 52, Nature Publishing Group; **i**, ref. 21, APS; **j**, ref. 17, American Chemical Society; **k**, ref. 22, Wiley.

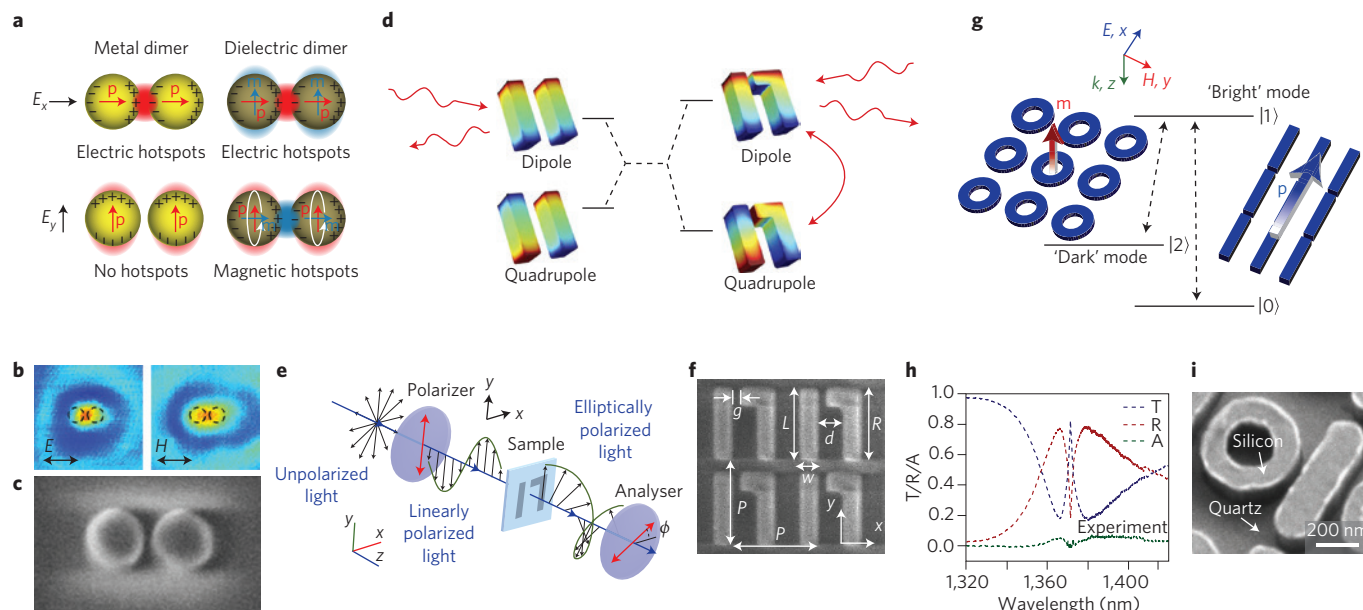


Figure 3 | Coupled all-dielectric resonators. **a**, Electric and magnetic hotspots using nanodimers. In coupled plasmonic nanoparticles, there is an electric field (E) hotspot inside the gap when the incident light is polarized parallel to the dimer axis. In dielectric resonators, this electric hotspot exists, but another magnetic hotspot can also exist for normal polarizations²⁸. p and m represent electric and magnetic dipole moments, respectively. **b**, Near-field scanning optical microscopy images revealing the electric and magnetic (H) intensity hotspots²⁸. The dashed circles represent the nanodimers. **c**, Scanning electron microscopy image of all-dielectric nanodimers composed of silicon nanodiscs with a radius of 140 nm and height of 150 nm. The gap size is 30 nm (ref. 28). **d**, Schematic representation of Fano interference between the electric dipolar and quadrupolar modes of pairs of silicon rods due to symmetry breaking²⁵. Red wavy arrows denote coupling to free-space radiation for the dipolar mode. The red curved arrow represents the interaction between the dipole and quadrupole. **e**, A 2D array of Fano resonant elements acting as a chiral metasurface can manipulate the polarization of light²⁵. ϕ , polarization rotation angle. **f**, Physical dimensions: $P = 2.4 \mu\text{m}$, $w = 500 \text{ nm}$, $d = 700 \text{ nm}$, $g = 200 \text{ nm}$, $R = 2 \mu\text{m}$ and $1.6 \mu\text{m} < L < 2 \mu\text{m}$ (ref. 25). **g**, Schematic representation of the interference between the dark and bright Fano resonant modes of silicon rods and rings²⁴. **h**, This interaction causes electromagnetically induced transparency and sharp spectral features in the transmission (T), reflection (R) and absorption (A) spectra²⁴. **i**, Scanning electron microscopy image of silicon rods and rings²⁴. Figure adapted with permission from: **a–c**, ref. 28, American Chemical Society; **d–f**, ref. 25, Nature Publishing Group; **g–i**, ref. 24, Nature Publishing Group.

all-dielectric metasurfaces can also accumulate position-dependent phase delay to shape the emerging wavefront²². A striking range of 0 to 2π phase shift with 100% transmission is achievable for high-efficiency arbitrary beam shaping (Fig. 2k). Spectrally overlapping electric and magnetic Mie resonances also offer a route⁵⁷ to create low-loss negative-refractive-index media³.

Coupling between all-dielectric nanoresonators can lead to interesting phenomena similar to their metallic counterparts, but with significantly enhanced efficiency and unique functionalities (Fig. 3). Plasmonic dimers⁵⁸ consisting of coupled metallic nanoantennas support electric field hotspots and have been researched extensively for surface-enhanced Raman sensing of molecules^{59–62}, nonlinear optics⁶³ and quantum effects⁶⁴. However, the predominantly electric dipole nature of plasmonic resonances makes it difficult to achieve any enhancement of the magnetic field²⁸. Arrays of silicon dimers can lead to magnetic hotspots in which the magnetic field is enhanced by a factor of six for gap sizes of 30 nm due to interaction of the magnetic Mie resonances (Fig. 3a), as demonstrated using near-field scanning optical microscopy²⁸ (Fig. 3b).

Coupled all-dielectric nanoresonators can lead to metasurfaces with significant spectral selectivity and control over the quality factor (Q -factor) of resonances. Microcavities can support high- Q resonances but suffer from poor far-field coupling²⁵. On the other hand, photonic crystal resonances arising from guided modes that rely on interference between multiple periods of the crystal cannot be miniaturized²⁵ and are also sensitive to the orientation of the incoming radiation⁶⁵. All-dielectric metasurfaces can overcome a number of difficulties in this regard by exploiting Fano resonances⁶⁶. A Fano resonance is a characteristic sharp feature in the absorption

or transmission spectrum of a nanophotonic structure when bright and dark modes interact⁶⁷ (Fig. 3d,g). The best candidate for a bright mode is a spectrally broad dipolar resonance, as it can be excited from free space, whereas quadrupolar resonances are good examples of dark modes: they are spectrally sharp and because they couple weakly to the far field, radiative losses are negligible. Examples of structures that support such bright modes are silicon nanorods, which behave like a dipole antenna²⁴, while silicon rings or pairs²⁵ of silicon rods support dark quadrupolar modes (Fig. 3f,i). Breaking the symmetry of coupled nanoresonators using a bent rod²⁵ or unequal spacing²⁴ between adjacent elements leads to interference between the dipolar and quadrupolar modes, producing a Fano feature^{24,68,69}. The standard three-level model describing this interaction is shown in Fig. 3d,g: it consists of a ground state with no excitation ($|0\rangle$) and a bright dipolar mode ($|1\rangle$) radiatively coupled to a dark quadrupolar mode ($|2\rangle$). This three-level system is also a way to in-couple radiation to the otherwise dark mode through the excitation of the bright mode. These Fano resonant metasurfaces can generate nanoscale hotspots⁷⁰ from strong field concentration, as they are governed by near-field interaction²⁵, unlike photonic crystal guided resonances that rely on long-range interference effects⁷¹. All-dielectric metasurfaces with broken inversion symmetry²⁵ can also act as chiral media⁸ to form ultrathin circular polarizers in the mid-infrared frequency range for polarization-sensitive spectroscopy or infrared identification devices (Fig. 3e).

The field enhancement is lower than in plasmonic structures, but a significant advantage is the lack of dissipation. Furthermore, the electric field hotspot can be controlled to lie either inside or outside the resonator in the near-field environment²⁴. Owing to the strong

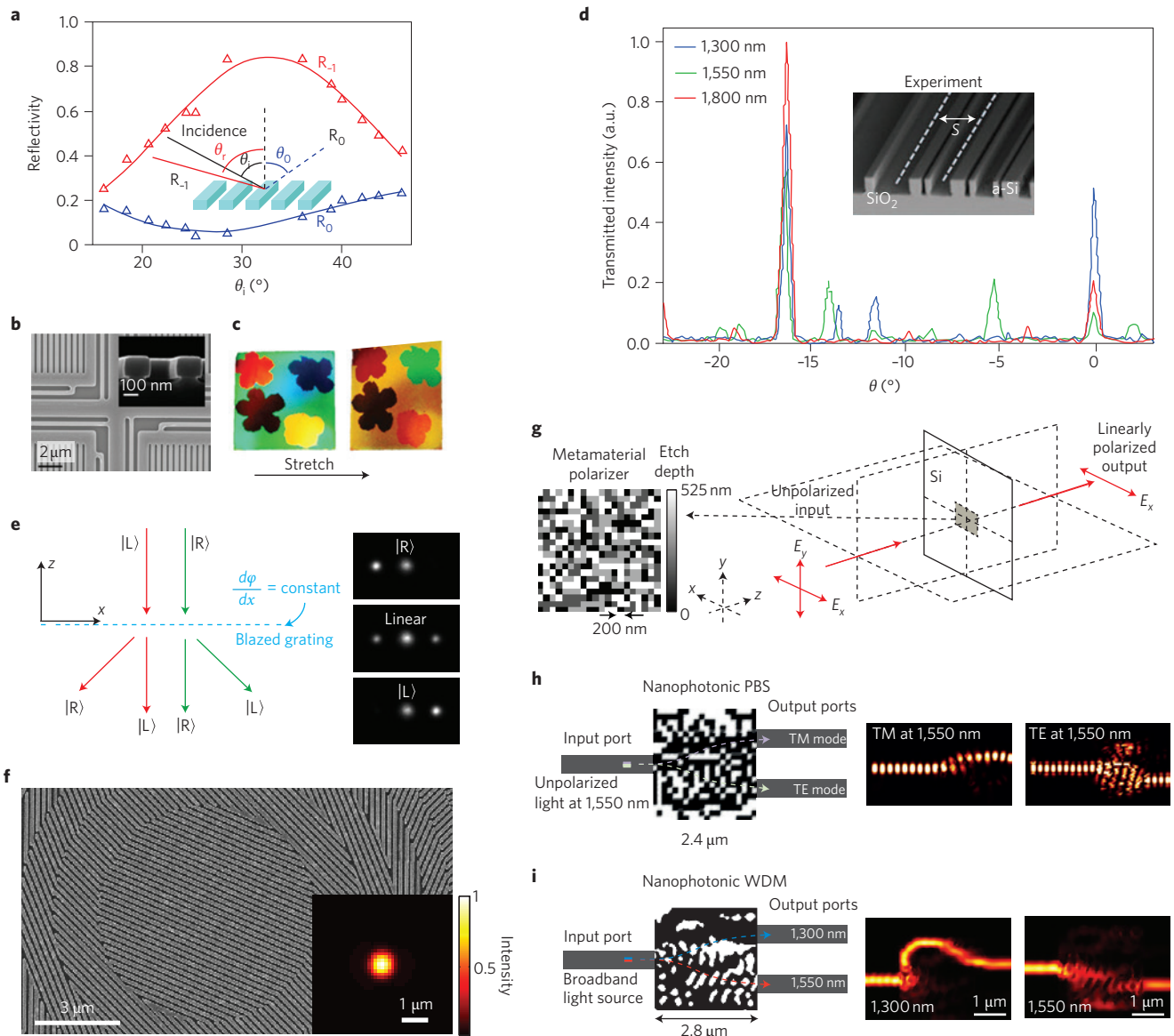


Figure 4 | All-dielectric metasurfaces. **a**, Using high-refractive-index contrast grating metasurfaces, it is possible to enhance the transmission or reflection (R) of one diffractive order ($m = -1$) while eliminating the rest to achieve vivid colours under white light illumination. The reflectivity dependence on the incident angle (θ) has been measured at 532 nm showing the stark contrast between R_{-1} and R_0 . These metasurfaces are composed of silicon nanorods with a thickness of 180–220 nm, period of 500–622 nm and duty cycle of 0.5, and are built on a stretchable substrate⁸². **b**, Scanning electron microscopy image of the high-contrast gratings. The inset shows the cross-section⁸². **c**, Stretching the substrate changes the structural colour on flower patterned gratings⁸². **d**, Achromatic metasurfaces are used to impart a constant phase gradient on a transmitted wave at multiple wavelengths. The metasurface is composed of coupled silicon rectangular resonators with a gap between them (inset). The height of the resonators and the period, S , of the grating are fixed while the resonator widths and slots sizes can be tuned. The transmitted light at 1,300, 1,550 and 1,800 nm is refracted by the same angle ($\sim 17^\circ$) (ref. 32). **e**, Schematic representation (left) and measured diffraction patterns (right) for an all-dielectric blazed grating with constant phase gradient. The metasurface is illuminated by right circular (R), linear, and left circular (L) polarization at $\lambda = 550$ nm. The blazed grating diffracts the incident light to the right or left depending on the incident polarization as shown in the images³¹. **f**, A fabricated flat lens using space-variant dielectric gradient metasurfaces. The focal point is 100 μm with numerical aperture of 0.43 at $\lambda = 550$ nm. The phase can be controlled by rotating the fast axis of the gratings. The lens is composed of eight discrete layers to approximate a hyperboloidal phase profile. This lens is illuminated by right circular polarized light and transforms it to left circular polarized light at the focal point. The spot size is 670 nm (full-width at half-maximum), which is close to the diffraction limit (inset)³¹. **g**, Metamaterial polarizer fabricated using an inverse-design computational approach. It transmits the desired polarization (E_x) unchanged and transforms the orthogonal polarization (E_y) to the desired polarization. Thus, the polarization conversion efficiency can reach 100%. Each unit cell is composed of 20×20 pixels with a size of 200×200 nm². A direct-binary-search optimization algorithm is used to find the proper etching depth for each silicon pixel⁹⁴. **h**, This method can be also used to design a polarization beamsplitter (PBS) as small as 2.4×2.4 μm^2 on a silicon-on-insulator platform that can separate transverse electric (TE) and transverse magnetic (TM) modes with the measured transmission efficiency of more than 70% and an extinction ratio of more than 11 dB (ref. 93). **i**, Another inverse-design approach has been used to yield a compact wavelength demultiplexer (WDM) on the silicon-on-insulator platform. The measured scattering parameters show relatively low insertion loss (2–4 dB) and a high extinction ratio (12–17 dB)⁹². Figure adapted with permission from: **a–c**, ref. 82, OSA; **d**, ref. 32, AAAS; **e, f**, ref. 31, AAAS; **g**, ref. 94, OSA; **h**, ref. 93, Nature Publishing Group; **i**, ref. 92, Nature Publishing Group.

Box 1 | Gratings with nanostructured unit cells for spectral and polarization control.

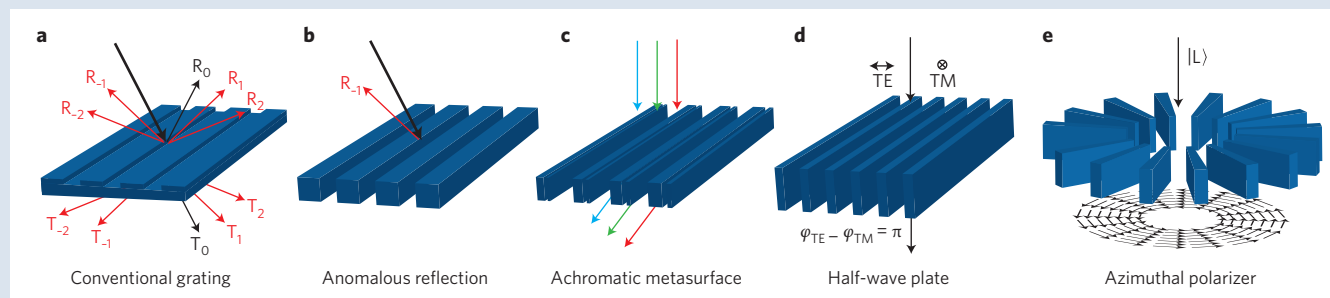
Conventional gratings are diffractive optical elements that exploit the constructive interference of specific wavelengths of incident radiation along fixed directions (panel **a**). Depending on the periodicity of the grating, the reflected (R) and transmitted (T) light are broken into multiple diffraction orders. Each diffraction order consists of a spectrum of wavelengths that have an angular spread (except the zeroth-order diffraction, which follows Snell's law). They are routinely used in optical elements to focus light or disperse the constituent colours of incident radiation.

Significant spectral control over the diffraction orders can be gained by carefully engineering the unit cell of the periodic diffracting structure (**b**). An array of two alternating media with very different refractive indices can enhance or suppress specific diffraction orders. In particular, when the periodicity is comparable to the wavelength of the incident light, only two diffraction orders are allowed in transmission and reflection: $m = 0$ and $m = -1$. The light passing through such gratings⁸² excites a series of waveguide modes in the nanobeams that couple to each other. Tuning the thickness and width of the grating results in an arbitrary control over the phase of the reflected and transmitted light. In particular, it is possible to suppress all diffraction orders other than R_{-1} resulting in anomalous reflection⁸².

Coupled rectangular dielectric resonators form the unit cell of gratings constituting achromatic metasurfaces³² (**c**). They consist of two silicon nanobeams separated by a slot with tunable widths and slot size. Light scattered from the coupled resonators and the field diffracted from the slot interfere in the far-field, and full 2π phase control can be achieved due to the resonant nature of the interaction³². This can lead to flat phase-shift profiles lacking any chromatic aberration over a broad range of wavelengths.

Deep-subwavelength silicon gratings are effectively anisotropic structures producing different phase shifts, ϕ , for transverse electric (TE) and transverse magnetic (TM) polarized light^{31,86,88,89} (**d**). This is similar to a standard birefringent calcite crystal with one important difference: the accumulated phase shift between the two field components over the same thickness can be two orders of magnitude higher due to the large index contrast between silicon and vacuum. The depth of the grating can be adjusted to accumulate a phase shift of π between the two electric field components, leading to an ultrathin half-wave plate⁸⁶. (The fundamental function of a half-wave plate is to rotate the incident linear polarization, whereas quarter-wave plates convert linear to circularly polarized light.)

The ultrathin half-wave plates described in **d** are anisotropic metacrystals with a slow optic axis along the nanobeams and a fast optic axis perpendicular to it. The grating vector is perpendicular to the parallel nanobeams. By spatially varying the grating vector, it is possible to change the local crystal axis in the plane of the grating³¹ (**e**). Thus, rotating the grating vector can imprint arbitrary rotations of the incident polarization. A subtle observation is that the thickness of the grating is constant while only the optic axis is changing. Thus, the dynamic phase accumulated for each point on the incident phase front due to propagation through the grating is exactly the same. However, an additional geometric phase (Pancharatnam–Berry phase) is imprinted at each point of the phase front depending solely on the local orientation of the optic axis⁸⁹. Therefore, a non-trivial phase modification is imparted to the transmitted light beam. Left circularly polarized incident beam ($|L\rangle$) generates an azimuthally polarized transmitted beam (**e**).



spectral selectivity of Fano features, all-dielectric resonators open multiple possibilities for biosensing of proteins⁷² and light-absorption enhancement in ultrathin materials, such as graphene^{25,71}, placed in the vicinity of the metasurface.

All-dielectric metasurfaces

Even though metamaterials research started with the quest for negative-index⁶, zero-index⁷, chiral⁷³ and hyperbolic⁷⁴ media, the goal of the field has grown into arbitrary control of the amplitude, phase and polarization of light waves at the subwavelength (nano) scale^{29,30}. The most promising route to achieve this goal consists of all-dielectric metasurfaces made of a thin layer of engineered silicon nanostructures (Fig. 4 and Box 1). These 2D surfaces can alter the wavefront of incident light for applications such as flat lenses^{75–77}, polarizers⁷⁸ and beam shaping^{54,79,80}. Their all-dielectric nature ensures higher transmission and diffraction efficiencies compared with plasmonic nanostructures.

Structural colour from metasurfaces can have a major impact on industrial applications as this approach sidesteps several drawbacks

of chemical dyes⁸¹ (Fig. 4a–c). By employing high-refractive-index contrast gratings made of silicon nanobeams, it was recently shown that the reflected light from a grating at specific wavelengths can propagate entirely towards the side of the incident beam⁸². This $m = -1$ diffraction order affects the perception of colour and its diffraction efficiency is strongly enhanced in the design. The periodicity, thickness and width of the nanobeams are chosen to suppress both the higher-order and the zeroth-order diffracted modes. This is evident in Fig. 4a, which shows the large reflection of the $m = -1$ order mode at 532 nm wavelength compared with the zeroth-order mode. Colour tuning can be achieved if the metasurface is fabricated on a stretchable membrane allowing the variation of the grating period (Fig. 4c and panels a,b in Box 1). Such high-contrast gratings can also form the basis for hollow-core waveguides⁸³ and ultra-broadband high-reflectivity mirrors⁸⁴.

Recent demonstrations have also shown the ability of metasurfaces to overcome chromatic aberration^{32,77} (Fig. 4d). Refractive optics, such as simple lenses, which bend light due to refractive-index changes, suffer from material dispersion and consequently,

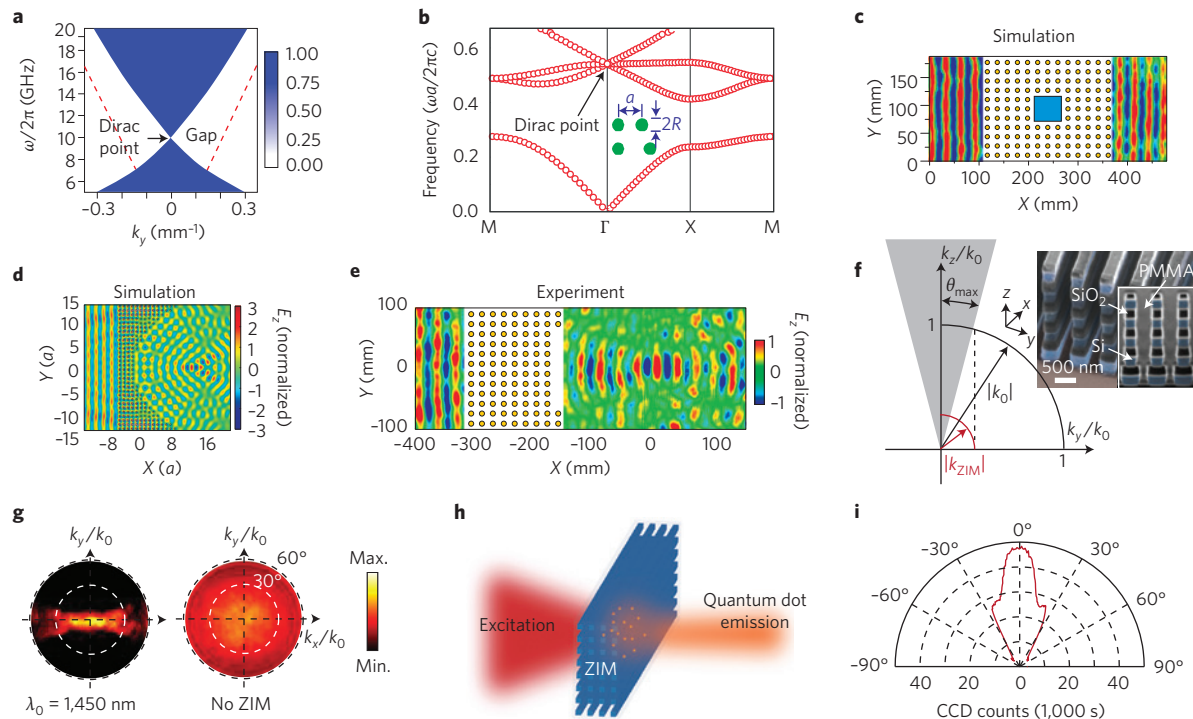


Figure 5 | All-dielectric zero-index metamaterials (ZIMs). **a**, Dispersion diagram of waves in an ideal dispersive plasma with electric and magnetic response. If the permittivity and permeability pass zero simultaneously, the dispersion is linear and cone-like near that frequency (ω). The blue regions denote propagating waves in the plasma and the white regions are beyond the light line of the plasma where no propagating waves are allowed. The permittivity and permeability have Drude dispersion with plasma frequency $f_D = \omega_D/2\pi = 10$ GHz and loss rate $\gamma = 10^{-5}$ GHz (ref. 101). **b**, Band diagram of an all-dielectric photonic crystal made of high-index rods. The Dirac cone at the Γ point can be induced by an accidental degeneracy mimicking the behaviour of zero-index media. The flat branch passing through the Dirac point (black arrow) is a longitudinal (bulk plasmon-like) magnetic mode. The photonic crystal is constructed from dielectric cylinders with $\epsilon = 12.5$ and radius $R = 0.2a$, where a is the periodicity. The critical difference from plasmonic realizations of ZIMs is that the group velocity does not go to zero when zero index is achieved¹⁸. **c**, Cloaking a metallic obstacle (blue rectangle) in ZIMs. The ZIM is composed of dielectric cylinders (yellow circles) with $\epsilon = 12.5$ inside a microwave parallel plate waveguide. The incident light frequency is set to be at the Dirac point with frequency $f = 0.541c/a$, where c is the speed of light in vacuum¹⁸. **d, e**, Simulations¹⁸ (**d**) and microwave experiments (**e**) depicting field distribution due to a concave-shaped surface on the zero-index photonic crystal. The focusing effect for incident plane waves confirms the zero phase change in transmission through a ZIM structure¹⁸. **f**, Experimental realization of ZIMs at optical frequencies. The structure is composed of vertically stacked silicon rods separated by SiO_2 layers. The rods have been fabricated from Si-SiO₂ multilayers and then patterned using reactive ion etching. The resulting air gaps have been filled by polymethylmethacrylate (PMMA) (inset). The isofrequency curve of a ZIM (inner red circular sector) has a much smaller radius than the vacuum isofrequency curve (black). The vertical dashed line is the largest possible projection of the ZIM isofrequency curve onto the vacuum isofrequency curve. This shows that only waves with parallel wavevectors (θ_{max}) within the shaded region can be coupled into ZIMs from free space making them very angularly selective¹⁹. **g**, Experimental Fourier-plane images of a beam passing through the fabricated ZIM at the Dirac point condition (left) and away from it (right) confirm the angular selectivity of the structure¹⁹. **h**, Schematic of experiment showing laser excitation of PbS quantum dots placed inside the ZIM¹⁹. **i**, Experimentally obtained highly directive spontaneous emission pattern of the PbS quantum dots (angular spread of 10°)¹⁹. CCD, charge-coupled device. Figure adapted with permission from: **a**, ref. 101, OSA; **b–e**, ref. 18, Nature Publishing Group; **f–i**, ref. 19, Nature Publishing Group.

different wavelengths focus at different spots. Diffractive optical elements, such as Fresnel lenses, which work based on the concept of interference of diffraction orders, have low efficiencies and are bulky. Optical metasurfaces, composed of an array of nanoresonators a fraction of a wavelength in thickness, can overcome these limitations by imparting strong phase changes that can be relatively constant over a broad spectral wavelength range. Initial designs of achromatic metasurfaces³² have shown that 240- μm -long silicon rectangular dielectric resonators can deflect normally incident light of various wavelengths in the same direction (Fig. 4d and panel c in Box 1). Future applications include achromatic lenses that can possibly replace flat Fresnel lenses, which are currently used in a multitude of applications, such as solar concentrators⁸⁵ and imaging systems⁵⁴.

Along with enhanced spectral control, metasurfaces can also affect the polarization and spatial profile of beams. This requires careful engineering of the orientation of the local grating vector^{86–88}. The basic building block to achieve this is the half-wave plate (panel d

in Box 1), which is the nanoscale adaptation of the textbook way of rotating linearly polarized light⁸⁶. If the optic axis of this nanophotonic half-wave plate is made to vary spatially, complex rotations of the incident waveform can be achieved (panel e in Box 1). Axicons (lenses that turn Gaussian beams into Bessel beams), blazed gratings, polarizers and waveplates were demonstrated recently on an all-dielectric silicon platform³¹ (Box 1). Similarly, unconventional optical elements that generate radial and azimuthally polarized beams from simple linearly polarized light have also been achieved (panel e in Box 1). Blazed gratings with phase that varies linearly across one grating period can be obtained solely from local polarization rotations on the metasurface. These polarization rotations are necessarily accompanied by accumulation of Pancharatnam–Berry phase, which are of geometric origin on the Poincaré sphere and unrelated to dynamic (propagation) phase^{89,90}. Figure 4e shows control over the diffracted polarization state of light with high efficiency using a linear phase gradient on the metasurface. Figure 4f shows the

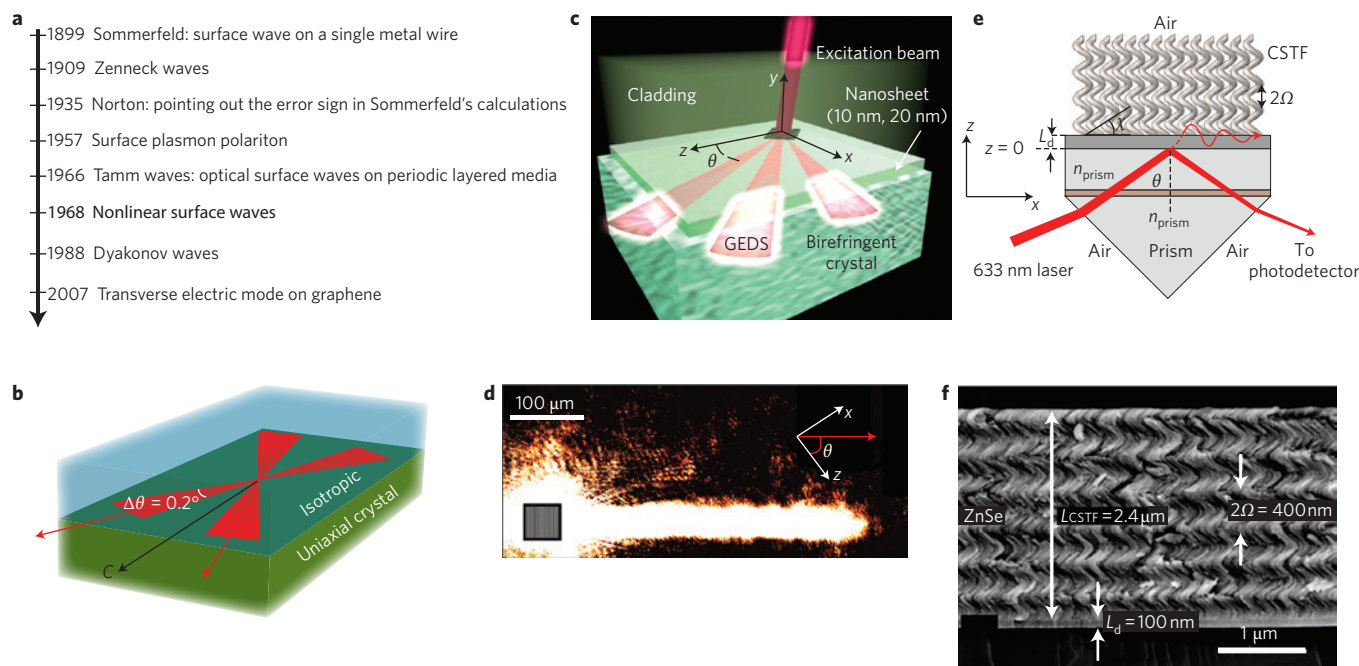


Figure 6 | Surface waves on all-dielectric media. **a**, Historical development of surface waves from the Zenneck¹⁰⁶ wave to the transverse electric surface mode on graphene¹¹⁰. A host of different media (metals¹⁴⁹, graphene¹¹⁰, nonlinear media^{108,109}, photonic crystals¹⁵⁰, anisotropic crystals¹³³) support surface waves. **b**, Schematic representation of Dyakonov surface waves along the interface between isotropic and anisotropic dielectrics. The optical axis of the anisotropic dielectric (C) is parallel to the interface and the surface wave propagates within a very narrow angular range ($\Delta\theta = 0.2^\circ$) for naturally anisotropic media. **c**, Guided modes enabled by Dyakonov surface waves (GEDS). If the two dielectrics are separated by a nanosheet, the widths of the angular existence domains increase to 1.48° and 3.88° , respectively. The structure is composed of a lithium triborate y-cut biaxial birefringent crystal ($n_x = 1.5743$, $n_y = 1.6015$, $n_z = 1.6160$ at $\lambda = 632.8$ nm), an Al_2O_3 nanosheet ($n = 1.7$) and liquid as a cladding. The propagation angle with respect to the optic axis changes from 56° to 62° when the cladding index changes from 1.601 to 1.607 (ref. 35). **d**, Image of the excitation beam coupled to the Dyakonov surface waves using a grating coupler³⁵. **e**, Dyakonov-Tamm wave. This surface wave can propagate along the interface between an anisotropic periodically inhomogeneous dielectric composed of chiral sculptured thin film (CSTF) with a structural period of Ω and an isotropic dielectric with a thickness of L_d . Unlike the Dyakonov waves, it can propagate in the entire 360° range. The existence of the wave was concluded through total internal reflection studies in a Kretschmann set-up using a prism (refractive index, $n_{\text{prism}} = 1.779$)¹¹⁴. **f**, Image of the periodic structure composed of upright parallel ZnSe nanohelices on a thin MgF_2 layer¹¹⁴. Figure adapted with permission from: **c,d**, ref. 35, Nature Publishing Group; **e,f**, ref. 114, APS.

scanning electron microscope image of nanobeams with differing orientations, which causes centrally symmetric polarization rotations of the incident beam. The accompanying centrally symmetric Pancharatnam–Berry phase accumulation causes a focal spot for incident light (inset). The all-dielectric Pancharatnam–Berry phase metasurface opens a multitude of future possibilities, including all-dielectric holographic plates⁹¹ with high efficiency and subwavelength thickness.

By envisioning metamaterials and metasurfaces as free-form structures with nanoscale pixels, it is possible to create any desired optical component^{92–95}. One device that is made possible by free-form all-dielectric metasurfaces is a highly efficient polarizer. Conventional polarizers reject the undesired polarization so their maximum efficiency is 50% when illuminated by unpolarized light. However, it was demonstrated that metamaterial polarizers can rotate the unpolarized light into the desired direction while simultaneously passing the desired polarization unchanged to achieve up to 74% efficiency⁹⁴ (Fig. 4g). Complex device design with desired functionalities can be first achieved computationally and then fabricated in silicon using focused ion beam milling. Remarkably, an all-dielectric metamaterial polarization beamsplitter was reported with a footprint as small as $2.4 \mu\text{m}$ by $2.4 \mu\text{m}$ (ref. 93, Fig. 4h) composed of 20 by 20 square pixels with sides of 120 nm. Each pixel can occupy two states: silicon or air. The photonic design methodology proceeds by a direct binary search algorithm with figures of merit defined to optimize the performance of the polarization beamsplitter. A

parallel development using inverse design was the demonstration of a compact all-dielectric wavelength splitter (Fig. 4i). The device has a footprint of $2.8 \mu\text{m}$ by $2.8 \mu\text{m}$ and splits light at $\lambda = 1,300$ nm and $\lambda = 1,550$ nm from a single input waveguide to two output waveguides⁹². Using this computational approach, all-dielectric metamaterials can be designed to meet the criteria for practical metadevices.

All-dielectric zero-index metamaterials

Zero-index metamaterials^{7,96} (ZIMs) have emerged as an important class of artificial media, because they show unique properties: cloaking⁹⁷, subwavelength waveguiding through bent channels⁹⁸, directional radiation patterns²³, infinite phase velocity and zero phase accumulation^{99,100}. They require epsilon-near-zero (ENZ; $\epsilon' \approx 0$) and mu-near-zero (MNZ; $\mu' \approx 0$) behaviour in the same spectral band. A fundamental advantage of ZIMs over ENZ or MNZ media is the wave impedance matching to vacuum, which leads to efficient in-coupling of light at normal incidence. While ENZ is routinely achieved at the plasma frequency (ω_p) of any metal ($\epsilon'(\omega_p) \approx 0$) or longitudinal optical frequency (ω_{LO}) of any polar dielectric ($\epsilon'(\omega_{LO}) \approx 0$), MNZ is significantly more difficult to achieve at optical frequencies.

An ideal model of a plasma with Drude dispersion in both the electric and magnetic response shows the intimate connection between Dirac cones and zero-index media¹⁰¹ (Fig. 5a). Surprisingly, the energy–momentum (E – k) dispersion of photonic waves in such a plasma shows a double coned structure (Fig. 5a) at $k = 0$. The passbands correspond to waves within the light line of the isotropic

Box 2 | Relaxed total internal reflection and evanescent wave skin-depth engineering³⁶.

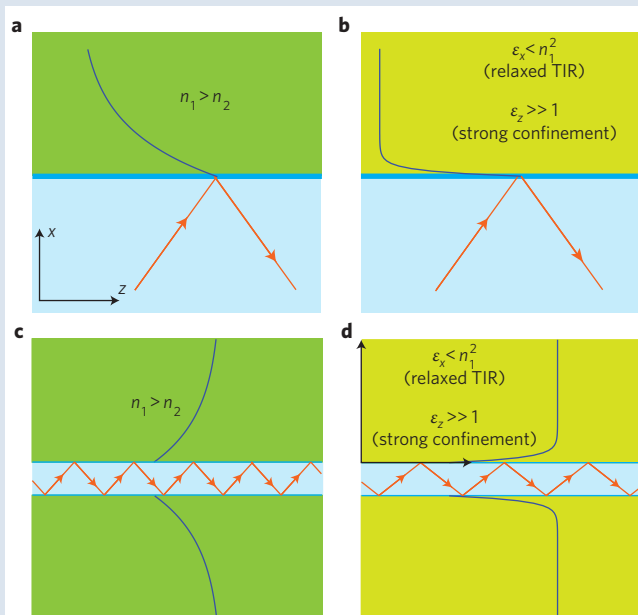
When an optical ray traverses a flat interface between two different isotropic dielectrics, light is partially reflected back to the first medium and is partly refracted in the second medium. Snell's law governs the angle of reflection and refraction. If $n_1 > n_2$ ($n_{1,2}$ is the refractive index of the two dielectrics) and the incident angle is greater than the critical angle ($\theta_c = \sin^{-1}(n_2/n_1)$), light is totally reflected back to the first medium and evanescently decays in the second medium (panel **a**). This phenomenon is known as total internal reflection (TIR).

However, if the second medium is anisotropic (optical axis is perpendicular to the interface) and the incident light is *p*-polarized (transverse magnetic mode), the TIR condition is reduced to $n_1 > n_{2x}$, a condition called relaxed TIR because it leaves a degree of freedom to choose the refractive index in the other direction³⁶. By increasing the refractive index in the parallel direction ($n_{2z} \gg 1$), it is possible to control the momentum and skin depth of the evanescent waves in the second medium:

$$k_{2x}^\perp = \frac{n_{2z}}{n_{2x}} \sqrt{(k_0 n_{2x})^2 - (k_z^\parallel)^2}$$

where $k_z^\parallel = n_1 k_0 \sin \theta$ is the tangential momentum of light and θ is the incident angle. Increasing n_{2z}/n_{2x} gives rise to reduced skin-depth in the second medium (**b**). Note that n_{2z} can even be greater than n_1 . Thus, extremely small skin-depth is achievable even if the incident light is in a low-index dielectric.

TIR is the fundamental phenomenon for confining light in conventional dielectric waveguides (**c**). However, when the core size of a dielectric waveguide is decreased, the evanescent field decays slowly in the claddings. At some point, the mode size becomes limited by the diffraction limit of light. If we cover a conventional dielectric waveguide with an anisotropic cladding,



the fundamental transverse magnetic mode of the waveguide still bounces off by relaxed TIR inside the core, but decays very fast outside³⁷. Thus, by increasing the anisotropy of the cladding, it is possible to confine a considerable amount of total power inside the subdiffraction core (**d**). Claddings with strong anisotropy can be realized using lossless all-dielectric metamaterials. Figure adapted with permission from ref. 36, OSA.

plasma. The singular Dirac point at the intersection of the two conical passband regions is related to the energy (frequency) that simultaneously achieves ENZ and MNZ. However, even if such an ideal plasmonic realization of ZIMs was achieved, it would suffer from high dissipation at the special Dirac point. This is because the group velocity (v_g) of such zero-index modes of plasmonic origin is low ($v_g \rightarrow 0$) even when the phase velocity (v_{ph}) is large ($v_{ph} = c/n \rightarrow \infty$), where c is the speed of light in vacuum. Intriguingly, all-dielectric non-plasmonic building blocks ($\epsilon > 1$) can be in principle used to achieve extreme parameters, including a vanishing refractive index.

One ingenious approach to achieve a ZIM without any plasmonic medium consists of creating Dirac points in an all-dielectric photonic crystal¹⁸. Dirac points are known to occur at Brillouin zone boundaries of photonic crystals¹⁰²; however, they do not possess properties of infinite phase velocity and zero phase accumulation during propagation — the hallmark of zero index. On the other hand, if a Dirac point with linear dispersion is engineered around $k = 0$, the photonic crystal starts exhibiting properties of ZIMs (Fig. 5b). The striking linear dispersion near $k = 0$ lends itself to an effective ZIM description far better than a similar effect at the zone boundary. This is because the lattice momentum is smaller at the zone centre so the effective wavelengths are larger allowing homogenization of the photonic crystal. This was recently achieved using an accidental degeneracy in the photonic band structure of a 2D crystal consisting of a square or triangular lattice of high-index dielectric rods¹⁸ (Fig. 5b, inset). This accidental degeneracy near $k = 0$ is different from conventional degeneracy due to symmetry that occurs in photonic crystals as conventional degeneracy leads to quadratic bands with zero group velocity, rather than linear Dirac-like dispersion.

Figure 5b shows the band diagram consisting of two branches with linear dispersion intersecting at a single point at $k = 0$.

Simulations of a scatterer placed inside a zero-index waveguide with perfect magnetic conductor boundary conditions¹⁸ show that the fields outside the zero-index medium are unaffected by the presence of the scatterer (Fig. 5c). Hence, it is cloaked⁹⁷. This is similar to the effect related to arbitrary-shaped channels filled with ENZ media, which show field tunnelling with no phase change (infinite phase velocity)⁹⁸. Figure 5d,e shows the simulation and experiment of a plane wave incident on a photonic crystal tuned to the frequency of zero index. The lack of phase propagation in the bulk and no phase variation along the edges of the photonic crystal implies that a concave-shaped surface would focus light to a spot.

Recently, this design was extended to the optical frequency range, where square cross-section silicon rods were embedded in a host matrix consisting of SiO₂ and polymethylmethacrylate, which have similar refractive indices¹⁹ (Fig. 5f, inset). It achieves a Dirac cone at the Γ point and zero-index behaviour at $\lambda = 1,450$ nm. Figure 5f compares the circular isofrequency relation for vacuum and the near-zero-index medium where the size of the circles are indicative of the indices. The narrow shaded region shows the range of angles of waves incident from vacuum, which are wavevector matched to the near-zero-index medium⁶⁶. Waves with off-normal incidence have a large impedance mismatch and are completely reflected. Figure 5g shows the experimental demonstration of this phenomenon using transmission measurements of light incident on the ZIM from free space. A narrow beam is observed in the Fourier plane at the zero-index wavelength of $\lambda = 1,450$ nm, while a broad angular spread is seen at wavelengths away from it. This effect can also be used to

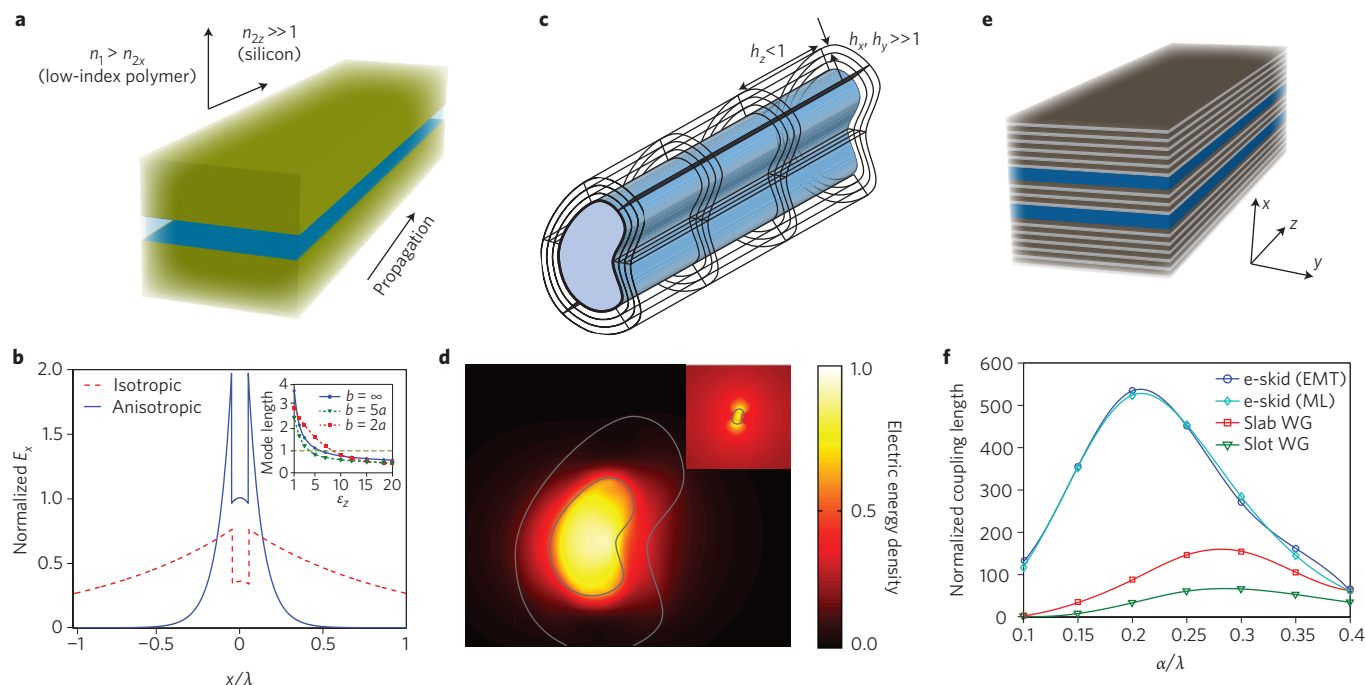


Figure 7 | Transparent subdiffraction photonics. **a**, Ideal 1D extreme skin-depth (e-skid) waveguide made of anisotropic claddings that behave like silicon in one direction and a low-index polymer in the other: if $n_1 > n_{2x}$ relaxed total internal reflection guarantees the propagation of the guided mode inside the core. If $n_{2z} \gg 1$, the momentum of evanescent waves in the cladding can be increased. Thus, the skin-depth decreases and the first transverse magnetic mode is strongly confined³⁷. **b**, Comparison of the calculated electric field of e-skid waveguides and slab waveguides. The core is glass with a size of 0.1λ . $\epsilon_x = 1.2$ in the cladding. Inset: Mode length versus dielectric constant in the direction perpendicular to the interfaces for various cladding sizes, where a and b are core and the cladding sizes, respectively. When $\epsilon_z > 7$, the mode length surpasses the diffraction limit of light³⁶. **c**, 2D e-skid waveguide. Schematic of the anisotropic cladding covering a waveguide with arbitrary cross-section³⁷. h_x, h_y, h_z correspond to coordinate expansions and compressions in the cladding. **d**, The comparison of electric energy density for an e-skid waveguide and conventional waveguide (inset) with the same core size shows that light is strongly confined inside the e-skid waveguide. The grey lines show the waveguide's boundaries. For the anisotropic cladding $\epsilon_x = \epsilon_y = 1.2$ and $\epsilon_z = 15$. The mode area and power confinement for the waveguide without cladding is $80(\lambda/2n_{\text{core}})^2$ and 1%, respectively, but the anisotropic cladding causes the mode area to reduce to $0.7(\lambda/2n_{\text{core}})^2$ and the power confinement increases to 36%³⁶. **e**, Practical realization of e-skid waveguides at telecommunication wavelength. Two coupled silicon waveguides (blue) with a size of 0.1λ and a centre-to-centre separation of 0.5λ . The cladding is composed of Ge-SiO₂ multilayer stacks (alternating dark and light grey) with germanium filling fraction of 0.6 (ref. 36). **f**, The calculated coupling length normalized to λ for e-skid waveguides (WGs) can be an order of magnitude larger than that in conventional slab waveguides with SiO₂ claddings. The large coupling length is indicative of low crosstalk and in slot waveguides, the crosstalk is larger than that in conventional waveguides³⁶. Also, there is good agreement between effective medium theory (EMT) and multilayer (ML) simulations. Figure adapted with permission from: **a**, ref. 37, OSA; **b,d-f**, ref. 36, OSA.

direct spontaneously emitted light from an ensemble of quantum emitters into a narrow cone of angles (Fig. 5h). Quantum dots tuned to emit in the spectral range of zero index produce a highly directional pattern (Fig. 5i). Even though zero index has been achieved at optical frequencies, miniaturization of such materials to form nanodevices is not possible as they rely on photonic crystal effects¹⁰³. It thus remains an important open question whether a metamaterial made of an array of high-index nanospheres can achieve zero-index properties.

Surface waves in anisotropic metamaterials

Surface photonic modes in all-dielectric media can be useful as information carriers at the nanoscale. Miniaturized photonic interconnects can allow information processing and communication at speeds beyond conventional electronics. However, the diffraction limit of light is a fundamental hurdle to miniaturization of waveguides, resonators and modulators¹⁰⁴. This has led to the emergence of plasmonics¹⁰⁵, where the surface wave consisting of electrons in a metal coupled with light can lead to a nanoscale mode volume conducive to miniaturization of optical devices. However, the dissipation losses of plasmonic devices are prohibitively high, making the on-chip power scaling with number of devices extremely inefficient.

It is therefore necessary to look for alternative surface waves that can act as a compact information carrier at the nanoscale.

In Fig. 6a, we outline the choices of surface waves for this ongoing search, including Zenneck–Sommerfeld^{106,107} waves, waves on the interface of a nonlinear medium^{108,109} and vacuum, and those on 2D materials such as graphene¹¹⁰. One class of surface waves that holds considerable promise for information processing due to their lossless nature are Dyakonov surface waves³³. These are waves at the interface of an isotropic medium ($n = n_{\text{iso}}$) and an anisotropic medium ($n = \{n_o, n_e\}$) when the crystal axis lies on the interface plane (Fig. 6b). The index along the crystal axis is denoted by n_e and the index in the plane perpendicular to it is n_o . Interestingly, these waves have a hybrid nature comprising of both transverse electric and transverse magnetic waves in the isotropic medium and extraordinary (e) and ordinary (o) waves in the anisotropic medium. In 1988, Mikhail Dyakonov came to the insightful conclusion that when $n_e > n_{\text{iso}} > n_o$, surface waves should exist on such an interface³³. This condition implies that the surface wave travels due to a counterintuitive condition of total internal reflection at both interfaces. However, one significant challenge is that the angle of existence of Dyakonov surface waves is less than 1° on the interface plane for naturally occurring anisotropic materials. This

is because natural uniaxial crystals (for example, TiO_2) have very weak anisotropy.

All-dielectric metamaterials can increase material anisotropy and in principle enable observation and control of Dyakonov waves^{34,35,111} in anisotropic waveguide structures. Dyakonov surface waves can induce guided modes in such structures even when all conventional bulk waveguide modes are cut-off. A thin nanosheet of alumina deposited on one side of a biaxial medium leads to nanoengineered Dyakonov surface waves that have a significantly enhanced angular range of existence on the interface plane. Liquids with different refractive indices can serve as a cladding on top of this anisotropic heterostructure for controlling the guided modes of Dyakonov surface waves³⁵ (Fig. 6c). A convincing study of the delicate condition of the existence of Dyakonov waves was performed by changing the index of the liquids used. Grating excitation of Dyakonov waves occurs with both transverse electric and transverse magnetic polarized input waves, consistent with the hybrid nature of the waves. Furthermore, the propagation direction changes drastically as the index of the liquid cladding layer is altered. This can be of vital importance in beam steering and photonic interconnect applications. The image of the beam of Dyakonov surface waves, out-scattered by surface inhomogeneities, is shown in Fig. 6d, which is similar to the beam-like behaviour observed for hybrid excitations of Dyakonov waves and surface plasmon polaritons^{112,113}. In principle, these guided Dyakonov modes are lossless, but surface inhomogeneities often reduce the propagation length. It is noteworthy that they offer the same confinement as long-range surface plasmon polaritons.

Another approach utilizing all-dielectric metamaterials to increase the angular range of Dyakonov-like waves was shown recently¹¹⁴. The approach uses two media, one isotropic and the other a sculpted thin film consisting of arrays of helically coiled ZnSe nanorods (Fig. 6e,f). This leads to a chiral anisotropic response and surface waves that can propagate in the entire 360° angular range. The deposition of the helical coiled nanorod arrays proceeds by a technique similar to glancing angle deposition¹¹⁵. The signature of these Dyakonov-like waves was observed in the reflection spectra using a Kretschmann geometry (Fig. 6e). These waves also have features common with Tamm waves, which exist at the interface of a truncated all-dielectric photonic crystal and an isotropic medium¹¹⁶. Tamm waves (Bloch surface waves¹¹⁷) propagate due to the photonic bandgap nature in one medium and total internal reflection in the other. Such Bloch surface waves are lossless and have field intensity maxima at the interface. They have been used as biosensors, because they can exhibit higher sensitivity than biosensing devices based on surface plasmon polaritons¹¹⁸.

Transparent subdiffraction photonics

Even though Dyakonov surface waves are promising for information processing, an important limitation is that their mode widths are not significantly below the wavelength. Decreasing the mode size is important for photonic interconnects⁸⁶ and to enhance quantum¹¹⁹ and nonlinear optical¹²⁰ responses. The diffraction limit is often considered as a fundamental hurdle in all-dielectric media, limiting the size of waveguides and resonators to roughly a cubic wavelength. Modern dielectric photonics uses total internal reflection¹²¹ as the fundamental principle to guide and confine light in optical fibres and resonators. For emerging nanoscale photonic devices, one significant limitation of total internal reflection is that it does not act on the evanescent waves that are inevitably generated at the interface. These unchecked evanescent waves extend far outside the core of a conventional optical fibre or a waveguide as the core size is decreased, making it impossible to achieve mode sizes significantly below the wavelength.

Recently, the principles of relaxed total internal reflection and evanescent wave skin-depth engineering were introduced to

significantly decrease the decay length of evanescent waves outside the core of a conventional waveguide³⁶ (Box 2). This requires the waveguide cladding to have a unique anisotropy that allows light to be completely reflected and simultaneously decrease the skin depth of the generated evanescent waves (Fig. 7a). The most significant advantage over plasmonic waveguides is the lack of dissipation, as the required indices in all directions are greater than one. This is a unique way of waveguiding, as the average index of the cladding is higher than that of the core, yet total internal reflection is preserved. Figure 7b shows the comparison of the field profile between the lowest-order transverse magnetic mode that propagates without cut-off in a 1D waveguide with and without the anisotropic cladding. A dramatic reduction in mode width to subdiffraction values is observed as the field decays rapidly in the anisotropic cladding.

The fundamental hybrid mode (HE₁₁) of an optical fibre or even an arbitrary-shaped waveguide can be confined far below the diffraction limit once the cladding is made anisotropic³⁷ (Fig. 7c). The anisotropic cladding ($\epsilon_x = \epsilon_y = 1.2$, $\epsilon_z = 15$) is far better than vacuum for field confinement inside the silica core causing a reduction of mode area by two orders of magnitude (Fig. 7d). Counterintuitively, the anisotropic cladding can also confine light better than a waveguide formed by a silicon/vacuum interface³⁷. This occurs as vacuum cannot change the penetration depth of the evanescent field.

The most promising approach to achieve this unique transparent high-contrast anisotropic metamaterial for 1D waveguides consists of a superlattice¹²² of silicon or germanium and silica (Fig. 7e). These interleaved multilayers with high and low index possess an effective uniaxial anisotropy with a crystal axis perpendicular to the layers (Box 2). This all-dielectric metamaterial can act as a cladding for the waveguide core made of silicon, leading to substantially enhanced power in the core and decreased mode sizes. The feature that distinguishes such extreme skin-depth (e-skid) waveguides from photonic crystal waveguides is the size of the layers, which are deeply subwavelength ($\lambda/10$). The mode is thus guided by total internal reflection and not photonic bandgap effects, which require the layer thicknesses to be tuned to $\lambda/4$. These e-skid waveguides are also fundamentally different from slot waveguides, which function on the basis of the field enhancement within slots surrounded by high-index silicon cores¹²³. The field outside slot waveguides decays extremely slowly in stark contrast to e-skid waveguides. This feature is detrimental and leads to crosstalk for closely spaced waveguides. The fundamental technological advantage of e-skid waveguides, compared with photonic crystal and slot waveguides, is the significant reduction in coupling between closely spaced waveguides arising from the fast decay of evanescent waves outside the core (Fig. 7f). Multilayer superlattices form the basis of multijunction solar cells¹²⁴, quantum cascade lasers¹²⁵ and quantum well photodetectors¹²⁶; therefore, engineering the evanescent field using all-dielectric metamaterials is well placed for integration with existing semiconductor optoelectronics.

Outlook

We envision several future directions in which the field of all-dielectric metamaterials can have a profound impact.

Biomimetic metasurfaces. Borrowing functionality from existing biomimetic structures¹²⁷ and adapting it to single-layer surfaces can be an important step to move towards applications. Recent demonstrations of nanophotonic structures that show reversal of colours in diffracted light, inspired by butterfly wings¹²⁸, can be implemented through ultrathin all-dielectric metasurfaces. The efficient anti-reflection coatings¹²⁹ important to solar cell and imaging technology have been previously designed¹³⁰, inspired by moth eyes that appear dark under white light illumination. An important goal would be to achieve the same functionality¹³¹ using a single layer

through an all-dielectric metasurface. Control of the polarization of light in reflection is a promising approach to camouflage inspired by silvery fish in water¹³². It has been demonstrated that scales of silvery fish, such as sardines, are optically anisotropic, consisting of layers with different crystal axes orientations. Subwavelength gratings are inherently anisotropic and the rotation of optic axes forms the basis of Pancharatnam–Berry phase polarization gratings^{86,89}. It is thus, in principle, possible to implement biomimetic polarization functionalities similar to fish scales through metasurfaces. A related goal would be to design metasurfaces to control Brewster angles and achieve broadband optical angular selectivity¹³³.

Quantum photonics. Another important direction is related to coupling of single emitters with all-dielectric nanoresonators and metamaterials^{134,135}. The electric field concentration in coupled all-dielectric nanoantennas is ideal for enhancing and controlling spontaneous emission from quantum dots. In addition, the directional nature of scattering when electric and magnetic resonances overlap¹⁷ can significantly enhance the collection efficiency for single photon sources¹³⁶. One main challenge here is integrating single emitters, such as nitrogen–vacancy centres in diamond¹³⁷, with all-dielectric nanoantennas and simultaneously tuning the Mie resonance to the wavelength of spontaneous emission. The magnetic field enhancement in silicon dimers could be used to increase the emission from magnetic dipole transitions in emitters such as Eu³⁺ that have low intrinsic quantum efficiency compared with spontaneous emission from emitters with electric dipole character^{138,139}.

Thermal photonics. An emerging theme in metamaterial research is the control of heat radiation for coherent thermal sources^{140–144}, thermophotovoltaics^{145,146} and high-temperature plasmonic coatings^{147,148}. Especially in the mid-infrared range, spectrally tailored thermal sources can lead to biosensing applications²⁵. All-dielectric Fano resonant chiral metasurfaces could be an approach to imprint polarization sensitivity and spectral selectivity to thermal emission, which is otherwise incoherent and unpolarized. More exotic thermal sources consisting of circularly polarized emission would find applications in infrared identification devices²⁵.

Silicon-on-insulator platforms. One significant advantage of all-dielectric anisotropic metamaterials is the possibility to fabricate them on-chip in a traditional, complementary metal–oxide–semiconductor (CMOS)-compatible silicon photonics platform to interface with existing photonic devices. Existing designs consisting of deep-subwavelength silicon gratings or multilayer silicon–silica superlattices cannot independently control the response to transverse electric and transverse magnetic polarized light. Consequently, the index contrast between these two polarizations is low. An ideal medium would have a response close to vacuum in one direction and that of silicon in the orthogonal direction. Achieving such an all-dielectric metacrystal would lead to practical devices, such as subdiffraction waveguides, holographic plates, polarizers and half-wave plates. Precise 3D positioning of high-index nanoresonators will be instrumental in achieving this objective.

Received 2 July 2015; accepted 23 November 2015;
published online 7 January 2016

References

- Maier, S. A. & Atwater, H. A. Plasmonics: localization and guiding of electromagnetic energy in metal/dielectric structures. *J. Appl. Phys.* **98**, 011101 (2005).
- Kittel, C. *Introduction to Solid State Physics* (Wiley, 2004).
- Soukoulis, C. M. & Wegener, M. Past achievements and future challenges in the development of three-dimensional photonic metamaterials. *Nature Photon.* **5**, 523–530 (2011).
- Schuller, J. A., Zia, R., Taubner, T. & Brongersma, M. L. Dielectric metamaterials based on electric and magnetic resonances of silicon carbide particles. *Phys. Rev. Lett.* **99**, 107401 (2007).
- Grigorenko, A. N. *et al.* Nanofabricated media with negative permeability at visible frequencies. *Nature* **438**, 335–338 (2005).
- Shalaev, V. M. Optical negative-index metamaterials. *Nature Photon.* **1**, 41–48 (2007).
- Silveirinha, M. & Engheta, N. Design of matched zero-index metamaterials using nonmagnetic inclusions in epsilon-near-zero media. *Phys. Rev. B* **75**, 075119 (2007).
- Hentschel, M., Schäferling, M., Weiss, T., Liu, N. & Giessen, H. Three-dimensional chiral plasmonic oligomers. *Nano Lett.* **12**, 2542–2547 (2012).
- Plum, E. *et al.* Metamaterial with negative index due to chirality. *Phys. Rev. B* **79**, 035407 (2009).
- Krishnamoorthy, H. N. S., Jacob, Z., Narimanov, E., Kretschmar, I. & Menon, V. M. Topological transitions in metamaterials. *Science* **336**, 205–209 (2012).
- Cai, W. & Shalaev, V. *Optical Metamaterials: Fundamentals and Applications* (Springer Science and Business Media, 2009).
- Zheludev, N. I. & Kivshar, Y. S. From metamaterials to metadevices. *Nature Mater.* **11**, 917–924 (2012).
- Joannopoulos, J. D., Johnson, S. G., Winn, J. N. & Meade, R. D. *Photonic Crystals: Molding the Flow of Light* 2nd edn (Princeton Univ. Press, 2011).
- Lewin, L. The electrical constants of a material loaded with spherical particles. *J. Inst. Electr. Eng. Part III Radio Commun. Eng.* **94**, 65–68 (1947).
- Evlyukhin, A. B. *et al.* Demonstration of magnetic dipole resonances of dielectric nanospheres in the visible region. *Nano Lett.* **12**, 3749–3755 (2012).
- Kuznetsov, A. I., Miroshnichenko, A. E., Fu, Y. H., Zhang, J. & Luk'yanchuk, B. Magnetic light. *Sci. Rep.* **2**, 492 (2012).
- Staudé, I. *et al.* Tailoring directional scattering through magnetic and electric resonances in subwavelength silicon nanodisks. *ACS Nano* **7**, 7824–7832 (2013).
- Huang, X., Lai, Y., Hang, Z. H., Zheng, H. & Chan, C. T. Dirac cones induced by accidental degeneracy in photonic crystals and zero-refractive-index materials. *Nature Mater.* **10**, 582–586 (2011).
- This paper proposes an all-dielectric zero-index medium without using plasmonic components.**
- Moitra, P. *et al.* Realization of an all-dielectric zero-index optical metamaterial. *Nature Photon.* **7**, 791–795 (2013).
- This paper reports the first experimental realization of an all-dielectric zero-index metamaterial at optical frequencies.**
- Liu, S. *et al.* Optical magnetic mirrors without metals. *Optica* **1**, 250–256 (2014).
- Pfeiffer, C. & Grbic, A. Metamaterial Huygens' surfaces: tailoring wave fronts with reflectionless sheets. *Phys. Rev. Lett.* **110**, 197401 (2013).
- Decker, M. *et al.* High-efficiency dielectric Huygens' surfaces. *Adv. Opt. Mater.* **3**, 813–820 (2015).
- This paper demonstrates that overlapping electric and magnetic resonances of equal strength can lead to highly directional and efficient Huygens sources.**
- Alù, A., Silveirinha, M. G., Salandrino, A. & Engheta, N. Epsilon-near-zero metamaterials and electromagnetic sources: tailoring the radiation phase pattern. *Phys. Rev. B* **75**, 155410 (2007).
- Yang, Y., Kravchenko, I. I., Briggs, D. P. & Valentine, J. All-dielectric metasurface analogue of electromagnetically induced transparency. *Nature Commun.* **5**, 5753 (2014).
- Wu, C. *et al.* Spectrally selective chiral silicon metasurfaces based on infrared Fano resonances. *Nature Commun.* **5**, 3892 (2014).
- Zhang, J., Liu, W., Zhu, Z., Yuan, X. & Qin, S. Strong field enhancement and light-matter interactions with all-dielectric metamaterials based on split bar resonators. *Opt. Express* **22**, 30889–30898 (2014).
- Kim, S. J., Fan, P., Kang, J.-H. & Brongersma, M. L. Creating semiconductor metafilms with designer absorption spectra. *Nature Commun.* **6**, 7591 (2015).
- Bakker, R. M. *et al.* Magnetic and electric hotspots with silicon nanodimers. *Nano Lett.* **15**, 2137–2142 (2015).
- This paper explains the fundamental difference in hotspots created by plasmonic and all-dielectric silicon nanodimers.**
- Yu, N. & Capasso, F. Flat optics with designer metasurfaces. *Nature Mater.* **13**, 139–150 (2014).
- Kildishev, A. V., Boltasseva, A. & Shalaev, V. M. Planar photonics with metasurfaces. *Science* **339**, 1232009 (2013).
- Lin, D., Fan, P., Hasman, E. & Brongersma, M. L. Dielectric gradient metasurface optical elements. *Science* **345**, 298–302 (2014).
- This manuscript reports wavefront and polarization manipulation of light using all-dielectric silicon based metasurfaces.**

32. Aieta, F., Kats, M. A., Genevet, P. & Capasso, F. Multiwavelength achromatic metasurfaces by dispersive phase compensation. *Science* **347**, 1342–1345 (2015).
33. Dyakonov, M. I. New type of electromagnetic wave propagating at an interface. *Sov. Phys. JETP* **67**, 714–716 (1988).
34. Artigas, D. & Torner, L. Dyakonov surface waves in photonic metamaterials. *Phys. Rev. Lett.* **94**, 013901 (2005).
35. Takayama, O., Artigas, D. & Torner, L. Lossless directional guiding of light in dielectric nanosheets using Dyakonov surface waves. *Nature Nanotech.* **9**, 419–424 (2014).
This paper reports the observation and control of Dyakonov surface waves in nanometre-thick films sandwiched between a biaxial crystal and an isotropic liquid cladding.
36. Jahani, S. & Jacob, Z. Transparent subdiffraction optics: nanoscale light confinement without metal. *Optica* **1**, 96–100 (2014).
This paper demonstrates a light confinement strategy beyond the diffraction limit by altering total internal reflection and evanescent wave skin-depth engineering.
37. Jahani, S. & Jacob, Z. Photonic skin-depth engineering. *J. Opt. Soc. Am. B* **32**, 1346–1353 (2015).
38. Bohren, C. F. & Huffman, D. R. *Absorption and Scattering of Light by Small Particles* (John Wiley & Sons, 2008).
39. Popa, B.-I. & Cummer, S. A. Compact dielectric particles as a building block for low-loss magnetic metamaterials. *Phys. Rev. Lett.* **100**, 207401 (2008).
40. Peng, L. *et al.* Experimental observation of left-handed behavior in an array of standard dielectric resonators. *Phys. Rev. Lett.* **98**, 157403 (2007).
41. Zhao, Q. *et al.* Experimental demonstration of isotropic negative permeability in a three-dimensional dielectric composite. *Phys. Rev. Lett.* **101**, 027402 (2008).
42. Zhao, Q., Zhou, J., Zhang, F. & Lippens, D. Mie resonance-based dielectric metamaterials. *Mater. Today* **12**, 60–69 (December, 2009).
43. Zhou, J. *et al.* Saturation of the magnetic response of split-ring resonators at optical frequencies. *Phys. Rev. Lett.* **95**, 223902 (2005).
44. Ahmadi, A. & Mosallaei, H. Physical configuration and performance modeling of all-dielectric metamaterials. *Phys. Rev. B* **77**, 045104 (2008).
45. Ginn, J. C. *et al.* Realizing optical magnetism from dielectric metamaterials. *Phys. Rev. Lett.* **108**, 097402 (2012).
46. Moitra, P. *et al.* Large-scale all-dielectric metamaterial perfect reflectors. *ACS Photon.* **2**, 692–698 (2015).
47. Moitra, P., Slovick, B. A., Yu, Z. G., Krishnamurthy, S. & Valentine, J. Experimental demonstration of a broadband all-dielectric metamaterial perfect reflector. *Appl. Phys. Lett.* **104**, 171102 (2014).
48. Esfandyarpour, M., Garnett, E. C., Cui, Y., McGehee, M. D. & Brongersma, M. L. Metamaterial mirrors in optoelectronic devices. *Nature Nanotech.* **9**, 542–547 (2014).
49. Schwanecke, A. S. *et al.* Optical magnetic mirrors. *J. Opt. Pure Appl. Opt.* **9**, L1–L2 (2007).
50. Fedotov, V. A., Rogacheva, A. V., Zheludev, N. I., Mladyonov, P. L. & Prosvirnin, S. L. Mirror that does not change the phase of reflected waves. *Appl. Phys. Lett.* **88**, 091119 (2006).
51. Sievenpiper, D., Zhang, L., Broas, R. F. J., Alexopolous, N. G. & Yablonovitch, E. High-impedance electromagnetic surfaces with a forbidden frequency band. *IEEE Trans. Microw. Theory* **47**, 2059–2074 (1999).
52. Fu, Y. H., Kuznetsov, A. I., Miroshnichenko, A. E., Yu, Y. F. & Luk'yanchuk, B. Directional visible light scattering by silicon nanoparticles. *Nature Commun.* **4**, 1527 (2013).
This article demonstrates directional light scattering by spherical silicon nanoparticles in the visible spectral range arising from simultaneous excitation of both electric and magnetic Mie resonances.
53. Zywiets, U., Evlyukhin, A. B., Reinhardt, C. & Chichkov, B. N. Laser printing of silicon nanoparticles with resonant optical electric and magnetic responses. *Nature Commun.* **5**, 3402 (2014).
54. Aieta, F. *et al.* Aberration-free ultrathin flat lenses and axicons at telecom wavelengths based on plasmonic metasurfaces. *Nano Lett.* **12**, 4932–4936 (2012).
55. Liu, W., Miroshnichenko, A. E., Neshev, D. N. & Kivshar, Y. S. Broadband unidirectional scattering by magneto-electric core-shell nanoparticles. *ACS Nano* **6**, 5489–5497 (2012).
56. Person, S. *et al.* Demonstration of zero optical backscattering from single nanoparticles. *Nano Lett.* **13**, 1806–1809 (2013).
57. Holloway, C. L., Kuester, E. F., Baker-Jarvis, J. & Kabos, P. A double negative (DNG) composite medium composed of magnetodielectric spherical particles embedded in a matrix. *IEEE Trans. Antennas Propag.* **51**, 2596–2603 (2003).
58. Nordlander, P., Oubre, C., Prodan, E., Li, K. & Stockman, M. I. Plasmon hybridization in nanoparticle dimers. *Nano Lett.* **4**, 899–903 (2004).
59. Hayashi, S., Koh, R., Ichiyama, Y. & Yamamoto, K. Evidence for surface-enhanced Raman scattering on nonmetallic surfaces: copper phthalocyanine molecules on GaP small particles. *Phys. Rev. Lett.* **60**, 1085–1088 (1988).
60. Talley, C. E. *et al.* Surface-enhanced Raman scattering from individual Au nanoparticles and nanoparticle dimer substrates. *Nano Lett.* **5**, 1569–1574 (2005).
61. Cao, L., Fan, P. & Brongersma, M. L. Optical coupling of deep-subwavelength semiconductor nanowires. *Nano Lett.* **11**, 1463–1468 (2011).
62. Caldrola, M. *et al.* Non-plasmonic nanoantennas for surface enhanced spectroscopies with ultra-low heat conversion. *Nature Commun.* **6**, 7915 (2015).
63. Ko, K. D. *et al.* Nonlinear optical response from arrays of Au bowtie nanoantennas. *Nano Lett.* **11**, 61–65 (2010).
64. Savage, K. J. *et al.* Revealing the quantum regime in tunnelling plasmonics. *Nature* **491**, 574–577 (2012).
65. Fan, S. & Joannopoulos, J. D. Analysis of guided resonances in photonic crystal slabs. *Phys. Rev. B* **65**, 235112 (2002).
66. Luk'yanchuk, B. *et al.* The Fano resonance in plasmonic nanostructures and metamaterials. *Nature Mater.* **9**, 707–715 (2010).
67. Ye, J. *et al.* Plasmonic nanoclusters: near field properties of the Fano resonance interrogated with SERS. *Nano Lett.* **12**, 1660–1667 (2012).
68. Miroshnichenko, A. E. & Kivshar, Y. S. Fano resonances in all-dielectric oligomers. *Nano Lett.* **12**, 6459–6463 (2012).
69. Zhang, J., MacDonald, K. F. & Zheludev, N. I. Near-infrared trapped mode magnetic resonance in an all-dielectric metamaterial. *Opt. Express* **21**, 26721–26728 (2013).
70. Bharadwaj, P., Deutsch, B. & Novotny, L. Optical antennas. *Adv. Opt. Photon.* **1**, 438–483 (2009).
71. Piper, J. R. & Fan, S. Total absorption in a graphene monolayer in the optical regime by critical coupling with a photonic crystal guided resonance. *ACS Photon.* **1**, 347–353 (2014).
72. Wu, C. *et al.* Fano-resonant asymmetric metamaterials for ultrasensitive spectroscopy and identification of molecular monolayers. *Nature Mater.* **11**, 69–75 (2012).
73. Papakostas, A. *et al.* Optical manifestations of planar chirality. *Phys. Rev. Lett.* **90**, 107404 (2003).
74. Podolskiy, V. A. & Narimanov, E. E. Strongly anisotropic waveguide as a nonmagnetic left-handed system. *Phys. Rev. B* **71**, 201101 (2005).
75. Pors, A., Nielsen, M. G., Eriksen, R. L. & Bozhevolnyi, S. I. Broadband focusing flat mirrors based on plasmonic gradient metasurfaces. *Nano Lett.* **13**, 829–834 (2013).
76. Fattal, D., Li, J., Peng, Z., Fiorentino, M. & Beausoleil, R. G. Flat dielectric grating reflectors with focusing abilities. *Nature Photon.* **4**, 466–470 (2010).
77. Khorasaninejad, M. *et al.* Achromatic metasurface lens at telecommunication wavelengths. *Nano Lett.* **15**, 5358–5362 (2015).
78. Falcone, F. *et al.* Babinet principle applied to the design of metasurfaces and metamaterials. *Phys. Rev. Lett.* **93**, 197401 (2004).
79. Arbabi, A., Horie, Y., Bagheri, M. & Faraon, A. Dielectric metasurfaces for complete control of phase and polarization with subwavelength spatial resolution and high transmission. *Nature Nanotech.* **10**, 937–943 (2015).
80. Shalaei, M. I. *et al.* High-efficiency all-dielectric metasurfaces for ultracompact beam manipulation in transmission mode. *Nano Lett.* **15**, 6261–6266 (2015).
81. Gu, Z.-Z. *et al.* Structural color and the lotus effect. *Angew. Chem. Int. Ed.* **42**, 894–897 (2003).
82. Zhu, L., Kapraun, J., Ferrara, J. & Chang-Hasnain, C. J. Flexible photonic metastructures for tunable coloration. *Optica* **2**, 255–258 (2015).
This article reports structural colour achieved using flexible, high-contrast grating metasurfaces.
83. Zhou, Y., Karagodsky, V., Pesala, B., Sedgwick, F. G. & Chang-Hasnain, C. J. A novel ultra-low loss hollow-core waveguide using subwavelength high-contrast gratings. *Opt. Express* **17**, 1508–1517 (2009).
84. Huang, M. C. Y., Zhou, Y. & Chang-Hasnain, C. J. A surface-emitting laser incorporating a high-index-contrast subwavelength grating. *Nature Photon.* **1**, 119–122 (2007).
85. Zhai, H., Dai, Y. J., Wu, J. Y., Wang, R. Z. & Zhang, L. Y. Experimental investigation and analysis on a concentrating solar collector using linear Fresnel lens. *Energ. Convers. Manag.* **51**, 48–55 (2010).
86. Levy, U., Tsai, C.-H., Pang, L. & Fainman, Y. Engineering space-variant inhomogeneous media for polarization control. *Opt. Lett.* **29**, 1718–1720 (2004).
87. Bomzon, Z., Biener, G., Kleiner, V. & Hasman, E. Radially and azimuthally polarized beams generated by space-variant dielectric subwavelength gratings. *Opt. Lett.* **27**, 285–287 (2002).
88. Sauvan, C., Lalanne, P. & Lee, M.-S. L. Broadband blazing with artificial dielectrics. *Opt. Lett.* **29**, 1593–1595 (2004).

89. Bomzon, Z., Kleiner, V. & Hasman, E. Pancharatnam–Berry phase in space-variant polarization-state manipulations with subwavelength gratings. *Opt. Lett.* **26**, 1424–1426 (2001).
90. Bomzon, Z., Biener, G., Kleiner, V. & Hasman, E. Space-variant Pancharatnam–Berry phase optical elements with computer-generated subwavelength gratings. *Opt. Lett.* **27**, 1141–1143 (2002).
91. Ni, X., Kildishev, A. V. & Shalae, V. M. Metasurface holograms for visible light. *Nature Commun.* **4**, 2807 (2013).
92. Piggott, A. Y. *et al.* Inverse design and demonstration of a compact and broadband on-chip wavelength demultiplexer. *Nature Photon.* **9**, 374–377 (2015).
93. Shen, B., Wang, P., Polson, R. & Menon, R. An integrated-nanophotonics polarization beamsplitter with $2.4 \times 2.4 \mu\text{m}^2$ footprint. *Nature Photon.* **9**, 378–382 (2015).
94. Shen, B., Wang, P., Polson, R. & Menon, R. Ultra-high-efficiency metamaterial polarizer. *Optica* **1**, 356–360 (2014).
95. Huntington, M. D., Lauhon, L. J. & Odom, T. W. Subwavelength lattice optics by evolutionary design. *Nano Lett.* **14**, 7195–7200 (2014).
96. Ziolkowski, R. W. Propagation in and scattering from a matched metamaterial having a zero index of refraction. *Phys. Rev. E* **70**, 046608 (2004).
97. Hao, J., Yan, W. & Qiu, M. Super-reflection and cloaking based on zero index metamaterial. *Appl. Phys. Lett.* **96**, 101109 (2010).
98. Silveirinha, M. & Engheta, N. Tunneling of electromagnetic energy through subwavelength channels and bends using ϵ -near-zero materials. *Phys. Rev. Lett.* **97**, 157403 (2006).
99. Mahmoud, A. M. & Engheta, N. Wave–matter interactions in epsilon-and-mu-near-zero structures. *Nature Commun.* **5**, 5638 (2014).
100. Li, Y. *et al.* On-chip zero-index metamaterials. *Nature Photon.* **9**, 738–742 (2015).
101. Wang, L.-G., Wang, Z.-G., Zhang, J.-X. & Zhu, S.-Y. Realization of Dirac point with double cones in optics. *Opt. Lett.* **34**, 1510–1512 (2009).
102. Mei, J., Wu, Y., Chan, C. T. & Zhang, Z.-Q. First-principles study of Dirac and Dirac-like cones in phononic and photonic crystals. *Phys. Rev. B* **86**, 035141 (2012).
103. Dong, J.-W. *et al.* Conical dispersion and effective zero refractive index in photonic quasicrystals. *Phys. Rev. Lett.* **114**, 163901 (2015).
104. Ozbay, E. Plasmonics: merging photonics and electronics at nanoscale dimensions. *Science* **311**, 189–193 (2006).
105. Schuller, J. A. *et al.* Plasmonics for extreme light concentration and manipulation. *Nature Mater.* **9**, 193–204 (2010).
106. Zenneck, J. Über die Fortpflanzung ebener elektromagnetischer Wellen längs einer ebenen Leiterfläche und ihre Beziehung zur drahtlosen Telegraphie. *Ann. Phys.* **328**, 846–866 (1907).
107. Sommerfeld, A. Ueber die Fortpflanzung elektrodynamischer Wellen längs eines Drahtes. *Ann. Phys.* **303**, 233–290 (1899).
108. Akhmanov, S. A., Sukhorukov, A. P. & Khokhlov, R. V. Self-focusing and diffraction of light in a nonlinear medium. *Sov. Phys. Uspekhi* **10**, 609–636 (1968).
109. Tomlinson, W. J. Surface wave at a nonlinear interface. *Opt. Lett.* **5**, 323–325 (1980).
110. Mikhailov, S. A. & Ziegler, K. New electromagnetic mode in graphene. *Phys. Rev. Lett.* **99**, 016803 (2007).
111. Takayama, O., Crasovan, L., Artigas, D. & Torner, L. Observation of Dyakonov surface waves. *Phys. Rev. Lett.* **102**, 043903 (2009).
112. Jacob, Z. & Narimanov, E. E. Optical hyperspace for plasmons: Dyakonov states in metamaterials. *Appl. Phys. Lett.* **93**, 221109 (2008).
113. High, A. A. *et al.* Visible-frequency hyperbolic metasurface. *Nature* **522**, 192–196 (2015).
114. Pulsifer, D. P., Faryad, M. & Lakhtakia, A. Observation of the Dyakonov-Tamm wave. *Phys. Rev. Lett.* **111**, 243902 (2013).
115. Robbie, K. & Brett, M. J. Sculptured thin films and glancing angle deposition: growth mechanics and applications. *J. Vac. Sci. Technol. A* **15**, 1460–1465 (1997).
116. Polo, J. A. & Lakhtakia, A. Surface electromagnetic waves: a review. *Laser Photon. Rev.* **5**, 234–246 (2011).
117. Liscidini, M. & Sipe, J. E. Analysis of Bloch-surface-wave assisted diffraction-based biosensors. *J. Opt. Soc. Am. B* **26**, 279–289 (2009).
118. Sinibaldi, A. *et al.* Direct comparison of the performance of Bloch surface wave and surface plasmon polariton sensors. *Sensor Actuat. B Chem.* **174**, 292–298 (2012).
119. Chen, X.-W., Sandoghdar, V. & Agio, M. Coherent interaction of light with a metallic structure coupled to a single quantum emitter: from superabsorption to cloaking. *Phys. Rev. Lett.* **110**, 153605 (2013).
120. Kauranen, M. & Zayats, A. V. Nonlinear plasmonics. *Nature Photon.* **6**, 737–748 (2012).
121. Hecht, J. *City of Light: The Story of Fiber Optics* (Oxford Univ. Press, 2004).
122. Herzog Sheinfux, H., Kaminer, I., Plotnik, Y., Bartal, G. & Segev, M. Subwavelength multilayer dielectrics: ultrasensitive transmission and breakdown of effective-medium theory. *Phys. Rev. Lett.* **113**, 243901 (2014).
123. Jahani, S. & Jacob, Z. Breakthroughs in photonics 2014: relaxed total internal reflection. *IEEE Photon. J.* **7**, 1–5 (2015).
124. Law, D. C. *et al.* Future technology pathways of terrestrial III–V multijunction solar cells for concentrator photovoltaic systems. *Sol. Energ. Mater. Sol. Cells* **94**, 1314–1318 (2010).
125. Faist, J. *et al.* Quantum cascade laser. *Science* **264**, 553–556 (1994).
126. Graf, M. *et al.* Terahertz range quantum well infrared photodetector. *Appl. Phys. Lett.* **84**, 475–477 (2004).
127. Sarikaya, M., Tamerler, C., Jen, A. K.-Y., Schulten, K. & Baneyx, F. Molecular biomimetics: nanotechnology through biology. *Nature Mater.* **2**, 577–585 (2003).
128. England, G. *et al.* Bioinspired micrograting arrays mimicking the reverse color diffraction elements evolved by the butterfly *Pierella luna*. *Proc. Natl Acad. Sci. USA* **111**, 15630–15634 (2014).
129. Huang, Y.-F. *et al.* Improved broadband and quasi-omnidirectional anti-reflection properties with biomimetic silicon nanostructures. *Nature Nanotech.* **2**, 770–774 (2007).
130. Sun, C.-H., Jiang, P. & Jiang, B. Broadband moth-eye antireflection coatings on silicon. *Appl. Phys. Lett.* **92**, 061112 (2008).
131. Spinelli, P., Verschuuren, M. A. & Polman, A. Broadband omnidirectional antireflection coating based on subwavelength surface Mie resonators. *Nature Commun.* **3**, 692 (2012).
132. Jordan, T. M., Partridge, J. C. & Roberts, N. W. Non-polarizing broadband multilayer reflectors in fish. *Nature Photon.* **6**, 759–763 (2012).
133. Shen, Y. *et al.* Optical broadband angular selectivity. *Science* **343**, 1499–1501 (2014).
134. Tame, M. S. *et al.* Quantum plasmonics. *Nature Phys.* **9**, 329–340 (2013).
135. Jacob, Z. Quantum plasmonics. *MRS Bull.* **37**, 761–767 (2012).
136. Lee, K. G. *et al.* A planar dielectric antenna for directional single-photon emission and near-unity collection efficiency. *Nature Photon.* **5**, 166–169 (2011).
137. Babinec, T. M. *et al.* A diamond nanowire single-photon source. *Nature Nanotech.* **5**, 195–199 (2010).
138. Noginova, N., Barnakov, Y., Li, H. & Noginov, M. A. Effect of metallic surface on electric dipole and magnetic dipole emission transitions in Eu^{3+} doped polymeric film. *Opt. Express* **17**, 10767–10772 (2009).
139. Taminiau, T. H., Karaveli, S., van Hulst, N. F. & Zia, R. Quantifying the magnetic nature of light emission. *Nature Commun.* **3**, 979 (2012).
140. Greffet, J.-J. *et al.* Coherent emission of light by thermal sources. *Nature* **416**, 61–64 (2002).
141. Krasnok, A. E., Miroshnichenko, A. E., Belov, P. A. & Kivshar, Y. S. All-dielectric optical nanoantennas. *Opt. Express* **20**, 20599–20604 (2012).
142. Filonov, D. S. *et al.* Experimental verification of the concept of all-dielectric nanoantennas. *Appl. Phys. Lett.* **100**, 201113 (2012).
143. Schmidt, M. K. *et al.* Dielectric antennas — a suitable platform for controlling magnetic dipolar emission. *Opt. Express* **20**, 13636–13650 (2012).
144. Schuller, J. A., Taubner, T. & Brongersma, M. L. Optical antenna thermal emitters. *Nature Photon.* **3**, 658–661 (2009).
145. Basu, S., Zhang, Z. M. & Fu, C. J. Review of near-field thermal radiation and its application to energy conversion. *Int. J. Energ. Res.* **33**, 1203–1232 (2009).
146. Celanovic, I., Jovanovic, N. & Kassakian, J. Two-dimensional tungsten photonic crystals as selective thermal emitters. *Appl. Phys. Lett.* **92**, 193101 (2008).
147. Molesky, S., Dewalt, C. J. & Jacob, Z. High temperature epsilon-near-zero and epsilon-near-pole metamaterial emitters for thermophotovoltaics. *Opt. Express* **21**, A96–A110 (2013).
148. Guler, U., Boltasseva, A. & Shalae, V. M. Refractory plasmonics. *Science* **344**, 263–264 (2014).
149. Ritchie, R. H. Plasma losses by fast electrons in thin films. *Phys. Rev.* **106**, 874–881 (1957).
150. Yeh, P., Yariv, A. & Hong, C.-S. Electromagnetic propagation in periodic stratified media. I. General theory. *J. Opt. Soc. Am.* **67**, 423–438 (1977).

Acknowledgements

The authors acknowledge funding from the Helmholtz Alberta Initiative and National Science and Engineering Research Council of Canada.

Additional information

Reprints and permission information is available online at www.nature.com/reprints. Correspondence and requests for materials should be addressed to Z.J.

Competing financial interests

The authors declare no competing financial interests.